HIGH TEMPERATURE OXIDATION OF ALUMINA FORMING CAST AUSTENITIC STAINLESS STEELS WITHIN AN ENVIRONMENT OF PURE STEAM

by

Elmer A. Prenzlow

A Thesis Submitted in

Partial Fulfillment of the

Requirements for the Degree of

Master of Science

in Engineering

at

The University of Wisconsin-Milwaukee

December 2016

ABSTRACT

HIGH TEMPERATURE OXIDATION OF ALUMINA FORMING CAST AUSTANITIC STAINLESS STEELS WITHIN AN ENVIRONMENT OF PURE STEAM

by

Elmer A. Prenzlow

The University of Wisconsin-Milwaukee, 2016
Under the Supervision of Dr. Benjamin C. Church

Steam cracking of hydrocarbons in the petrochemical industry is a multibillion dollar industry. The processes performed in these plants create byproducts that negatively affect the integrity of stainless steel piping through high temperature corrosion. Alloys used presently in industry rely on the formation of chromium oxide (chromia) as a protective layer between the bulk metal pipe and chemical byproducts. However, chromia can become susceptible to attack from aggressive species such as carbon, water vapor, and sulfur compounds, thus creating a need for a better protection method.

A new series of austenitic stainless steels have been developed in recent years that, rather than forming chromia, create a protective layer of aluminum oxide (alumina) under oxidative conditions. These alloys have high nickel content for the stabilization of the austenitic phase, and a more thermodynamically stable oxide layer relative to the traditional chromia formers. Consequently, alumina forming alloys have been proposed as replacements for chromia forming alloys in the petrochemical industry. General oxidation testing has been performed on alumina forming alloys under dry and 10% water vapor conditions. However, oxidation conditions in

industry resemble a 100% steam environment. Therefore, test methods to mimic such conditions are needed so that alloys can be tested and developed further for these applications.

Four alloys with aluminum contents ranging from 2.6 to 3.9 wt% were cut from centrifugally cast pipes and subjected to oxidation in an environment of pure steam for up to 30 hours, at temperatures of 800 °C and 950 °C. Samples were analyzed using Raman, SEM, and EDS and showed a continuous alumina layer free of cracks. The alumina layer thickness increased with time. Additionally, larger thicknesses were observed in samples oxidized at 950 °C from those of 800 °C. Thickness measurements were used to calculate parabolic and non-parabolic oxidation rate constants. Samples were compared using calculated parabolic and modified parabolic rates of oxidation. Plots for the prediction of oxide layer thickness were generated both for the Wagner model of parabolic oxidation, and an experimentally determined modification to said model. Oxide scale thickness as formed in pure steam was shown to be related to the aluminum content of the alloy and the temperature and time of exposure.

Further testing of alumina forming stainless steels in other concentrations of steam would allow for the determination of steam's effect on alumina formation kinetics. In addition, tests at additional temperatures between 800 and 950 °C would allow for the calculation of activation energies and full understanding of the oxide layer. Finally, the analysis of alumina layer thickness effects on coking performance in a petrochemical application would allow for the potential transition of these alloys into the commercial market.

To

My family,

Especially my grandfather, Wallace Karrasch

Their life work and support have made me the man I am today.

TABLE OF CONTENTS

LIST OF FIGURES

LIST OF TABLES

ACKNOWLEDGEMENTS

First, I would like to thank my advisor Dr. Ben Church for aiding and assisting me throughout my graduate studies. His guidance was invaluable in my completion of this degree and always had an open door. I would also like to thank Jim Myers of MetalTek for providing his industrial insight and resources regarding the applications involved throughout this project.

Additionally, I would like to thank a number of faculty for their time and resources made available to me over the course of these two years: Dr. Steven Hardcastle for training and guidance in the AAF, Dr. Hugo Lopez for knowledge gained through several of his classes and sitting on my defense committee, Dr. Benjamin Schultz for being a part of my defense committee and teaching me about foundry operations, and Dr. Heather Owen for training and assistance on the Hitachi scanning electron microscope.

Finally, I would like to thank my peers and research group members: Lizeth Ortiz, Shengyi Li, Kao Yang, and Bruna Dos Santos whose friendship and assistance were of great value to me throughout this program.

CHAPTER 1 – INTRODUCTION

1.1 Background

Pipes are the veins and arteries of the petrochemical industry, and similarly to a human's vascular system, they can become coated with undesirable substances. Although analogous, the process in which pipes become coated in an industrial plant are different from the ways of the human body. Instead of platelets sticking to the insides of arteries, chemical reactions occur during the process of thermal cracking that produce undesirable byproducts that can then form deposits on the pipe walls. The eventual buildup of these byproducts necessitates periodic cleaning processes resulting in down time and lost production. The formation of coke through the thermal cracking of hydrocarbons is termed coking. Coking results in a buildup on the inside surfaces of pipelines, that eventually reduce plant efficiency through pressure loss and heat transfer reduction (1).

In order to prevent coking, research into chemical additives has been performed, focusing on modifying the chemical reactions in the cracking environment in order to reduce the volume of coke produced (2). Coke formation can be slowed but is regarded as being unavoidable. The current procedure to remove coke buildup involves the shutdown of cracking operations. During shutdown, high temperature steam is passed through the system. The steam reacts with the carbon deposits to form CO2 and other light hydrocarbon gasses. In addition to the coke removal, the steam oxidation process will reform a protective oxide layer on the inside of the pipes.

Protective oxides which prevent high temperature corrosion from coke buildup are the current method utilized in these petrochemical plants. The layer is comprised of chromium oxide, and performs reliably under standard conditions. However, the chromium layer often

struggles in protecting the pipe in the presence of aggressive species such as water vapor, carbon, and sulfur (3). Because of these aggressive species being present in the cracking process, it is desired for a more effective oxide layer to be formed, one which can more effectively prevent coking.

A recent class of austenitic stainless steel alloys has been developed which, under high temperature oxidation conditions, form an aluminum oxide layer rather than a layer of chromium oxide as is the case with traditional alloys. This alumina layer is beneficial due to its increased thermodynamic stability in the presence of oxygen and aggressive species relative to chromia (3). However, there exists a need for the development of oxidation data that is capable of predicting alumina layer thickness in an environment directly comparable to the cleaning cycle used in industry. This data will allow for less down time of the plant, and a greater ability to predict the required time and temperature of an oxidation cycle.

1.2 Oxidation theory

In order to effectively develop a process which studies the oxidation of the steel pipes used in cracking plants, a fundamental understanding of oxidation kinetics is necessary. There are several kinetic models that can be considered when attempting to study the rate at which oxides develop. There are three main models: Linear, Parabolic, and Logarithmic which can be seen in Figure 1 (4), yet each model has its own set of conditions where it is applicable. For instance, the logarithmic rate law assumes that the rate at which the metal oxidizes is derived from a space charge layer limiting the flow of electrons from the metal to oxide layer creating an oxide which increases rapidly in thickness but dwindles as time passes. The logarithmic rate low

generally applies to oxidation at lower temperatures and metals of higher purity, thus making it unlikely to be useful for this application (5).

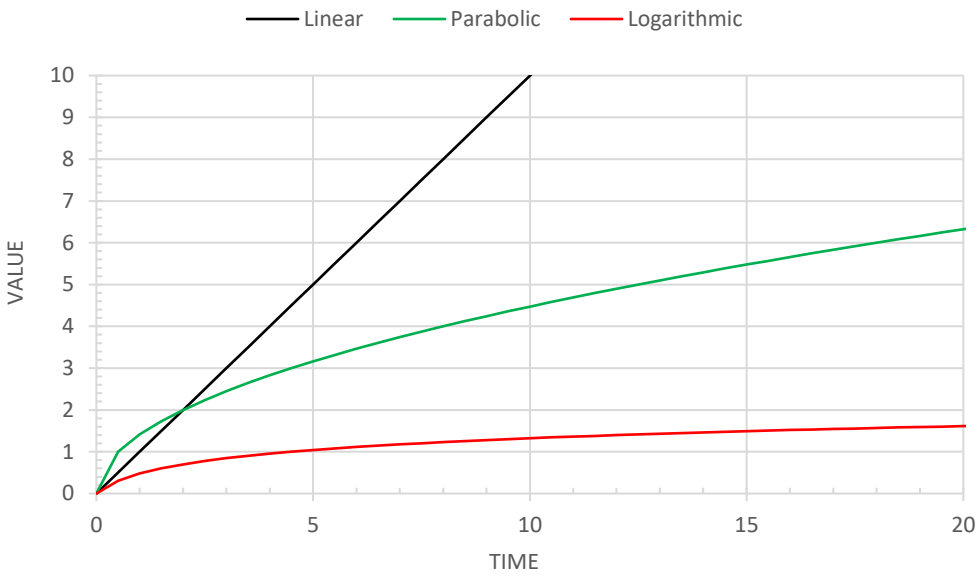

Figure 1: Types of rate models

On the other hand, the parabolic rate law or more commonly referred to as the Wagner Oxidation Model assumes that the rate at which the oxide layer develops is controlled by the diffusion of metallic and oxygen ions through the oxide layer (6). Unlike the logarithmic model, this model is applicable under high temperatures, allowing for its application in the design of this experiment.

The Wagner model of oxidation makes five assumptions (7)

1. "The oxide scale is compact and adherent.
2. Migration of charged species, ions, electrons, or electron holes are the rate controlling species
3. Thermodynamic equilibrium is established at both the metal/scale and scale/gas interface

4. The oxide is more or less stoichiometric
5. Oxygen solubility in the metal may be neglected"

The Wagner model can be derived starting with a generic rate law shown in Equation 1 which states that the change in thickness *x* with respect to time *t* is a function of thickness and time.

$$\frac{dx}{dt} = f(x,t) \qquad \textit{Equation 1}$$

Using the generic rate equation above, and making the assumption that the rate is parabolic, Equation 2 is produced where *kp* is the parabolic rate constant.

$$f(x,t) = k_p/2x \qquad \textit{Equation 2}$$

Integrating the parabolic rate equation with the relationship from Equation 2 results in Equation 3 which shows a relationship between the change in thickness and the change in time.

$$\Delta x = k_p \Delta t^{1/2} \qquad \textit{Equation 3}$$

Equation 3 is the fundamental relationship between oxide layer thickness and oxidation time under the Wagner model, where he showed that the rate determining step in an oxidation process is controlled by diffusion of ions through an oxide layer as shown in Figure 2. In addition, he showed that if the rate limiting step is indeed ion transfer then the resulting relationship will be parabolic (6). This model predicts that the growth rate of the oxide layer decreases with time. Eventually, the oxide layer will become stable, ceasing to grow.

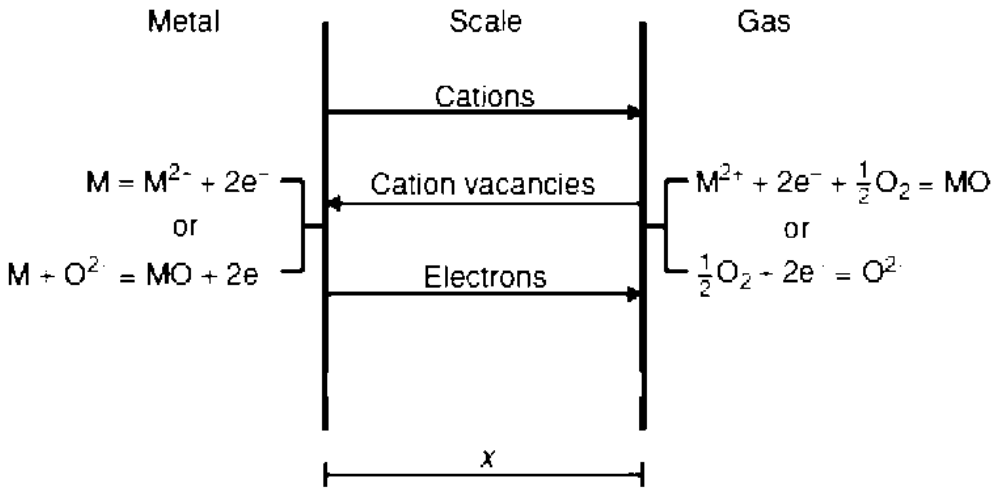

Figure 2: Wagner oxidation model illustration (8)

The Wagner model predicts a parabolic rate law with a time exponent of one half, however there is evidence that alumina scale has the potential to follow a modified Wagner model. Instead of an exponent of one half, theoretical modeling has shown that the exponent for alumina formation in dry air can develop at a rate where the exponent is less than one half. For example, the plot shown in Figure 3 shows a time exponent of 0.35 much less than that of the Wagner model, and is due to the inclusion of microstructural effects in the calculation of the oxidation kinetics (9).

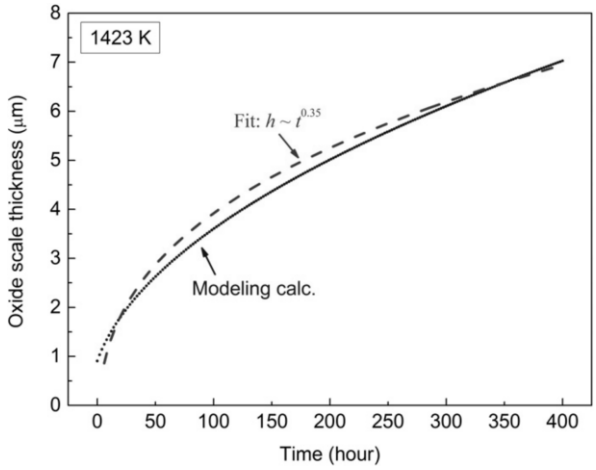

Figure 3: Modified Wagner model exponent for alumina scale theoretical modeling (9)

As it has been shown that alumina may not follow a standard Wagner model of oxidation, a method of calculating the time exponent and experimental rate constant is needed. In order to do this the parabolic rate law can be modified to Equation 4 to solve for the value of *n* based on experimental data and a linear regression.

$$ln(\Delta x) = n * l\,n(t) + ln(k_n) \qquad \textit{Equation 4}$$

1.3 Aluminum as an alloy addition

Alumina forming austenitic stainless steel alloys utilize aluminum to create a protective alumina layer for preventing corrosion much in the same way as traditional stainless steels use chromium. However, aluminum is a strong ferrite phase stabilizer when alloyed with iron thereby limiting the formation of gamma phase austenite (10). This can be seen in Figure 4, where there exists a very minute region in which an alloy of iron and aluminum under 1.95 at% would exist in austenitic phase (11). Additions of aluminum to a traditional stainless steel can be problematic and cause issues with processability, strengthening mechanisms, and microstructural stability/

In order to compensate for the effects of aluminum alloying additions, higher quantities of nickel are used while limiting amounts of chromium, aluminum, and niobium. Nickel is a valuable alloying addition due to its corrosion resistant benefits in addition to the austenite phase stabilization it provides. This effect can be seen in Figure 5, where there exists a region covering the entire diagram in which austenitic iron is created when alloyed with nickel (12). This would indicate that for any addition of ferrite stabilizers, an increased content of nickel would offset any negative phase formations. Nickel is not the only elemental modification that can be made.

Other austenite stabilizers such as manganese can be increased as can ferrite stabilizers such as chromium be decreased.

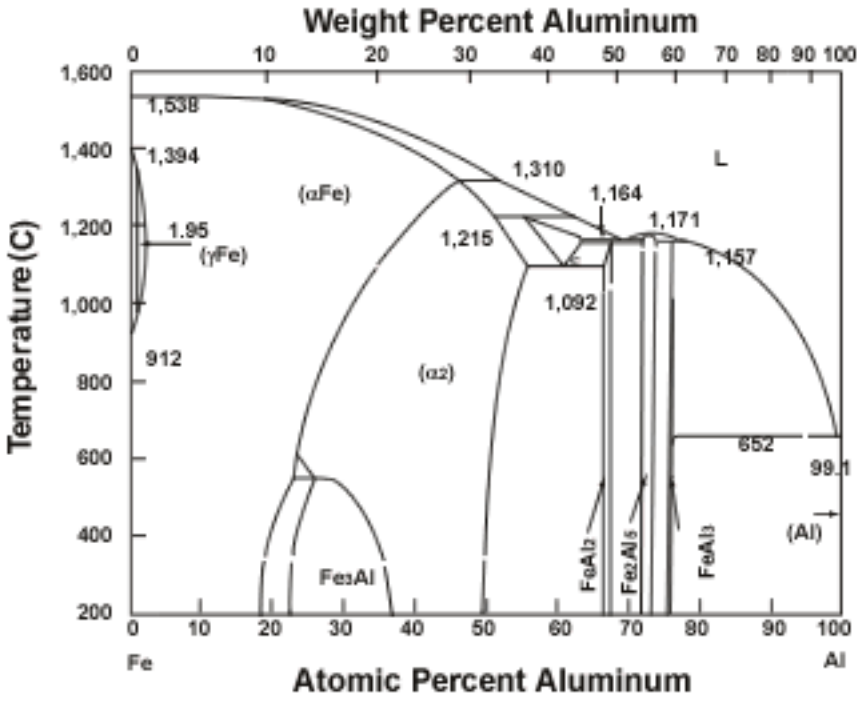

Figure 4: Iron aluminum phase diagram (11)

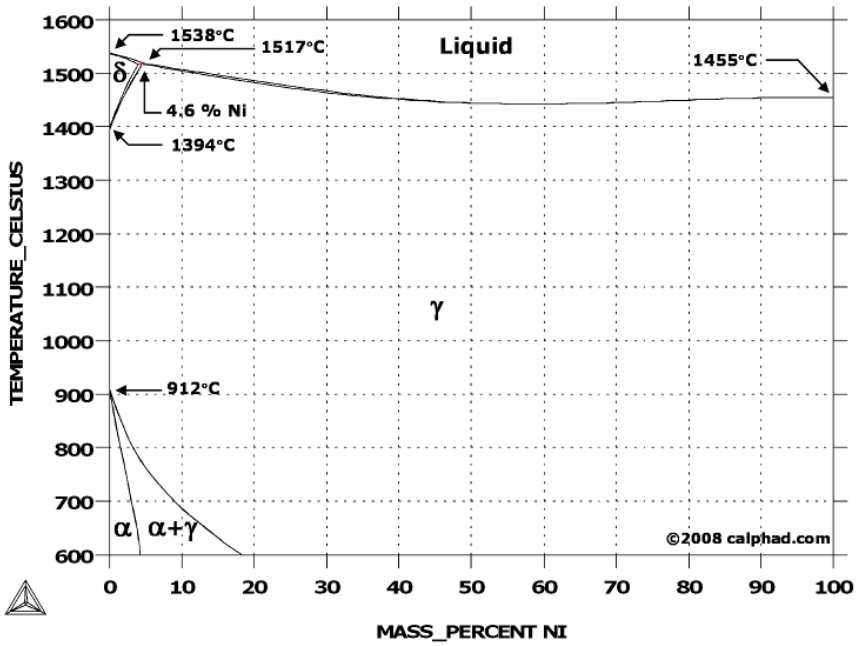

Figure 5: Iron nickel phase diagram (12)

1.4 Chromium oxide vs alumina forming alloys in petrochemical industry

Current petrochemical pipes are cast or wrought out of chromium oxide forming stainless steels (13). This is problematic due to the limitations that chromium oxide presents in the presence of aggressive species. These species include water vapor, carbon compounds, and sulphur compounds of which many varieties are present during operation of a steam cracking plant. In these plants the chromium oxide layer becomes compromised and allows the increased effect of coking due to accelerated degradation. The degradation is a direct result of volatile chromium oxyhydroxide and an increased tendency for internal oxidation (10). Coke formation kinetics can also be increased when the processing gas has direct contact with metal as opposed to an oxide layer barrier.

Unlike chromium oxide protected pipes, the aggressive species present in steam cracking plants have a drastically reduced effect on the pipes containing an aluminum oxide layer on their surface. This stems from the nature of aluminum oxide being considerably more stable than chromium oxide at high temperatures (3). However, the rate at which aluminum oxide develops is orders of magnitude lower than that of chromium oxide. A comparison of chromium oxide to aluminum oxide can be seen in Figure 6, and shows that the alumina is considerably better thermodynamically, assuming the reduction in growth rate is acceptable. The desired kinetics in this application are to have an initial fast oxide growth to protect the metal and then a greatly reduced rate such that alloy depletion of the base metal does not cause long-term degradation.

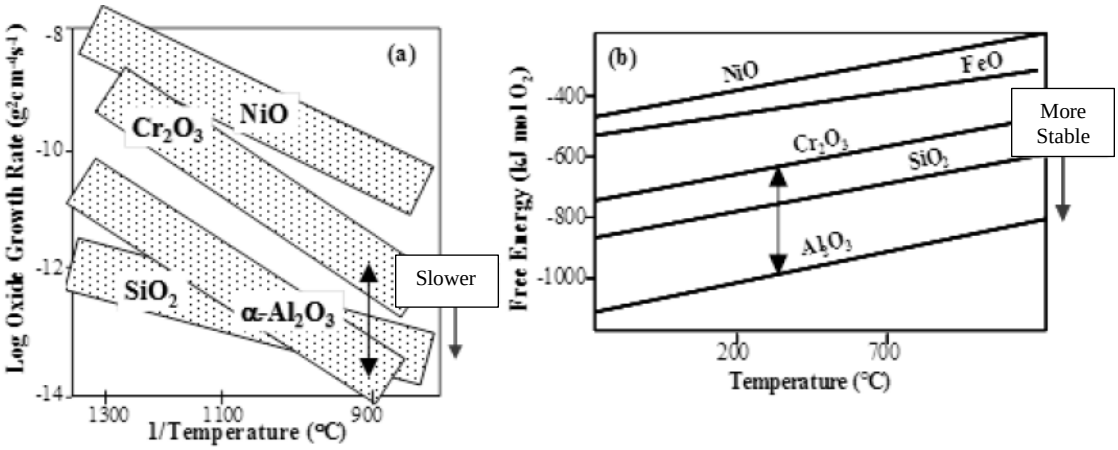

Figure 6: Growth rate and thermodynamic stability comparison of Cr & Al oxide (3)

Testing has been completed to show the benefit of alumina over chromia by the Oak Ridge Laboratory where samples were exposed to extended periods of time in cyclic oxidizing conditions. These experiments focused on a temperature of 800 °C in air with 10 vol% water, where it was determined that alloys containing aluminium did not suffer weight loss over time due to oxidation, but rather gained mass over time in accordance with the development of a protective alumina layer. These results can be seen in Figure 7, and show the dramatic loss of mass of the HK alloy containing 25 wt% Cr, and the gain of mass of alloys 1, 4, and 5, containing roughly 14 wt % Cr and 3.5 wt% Al (10).

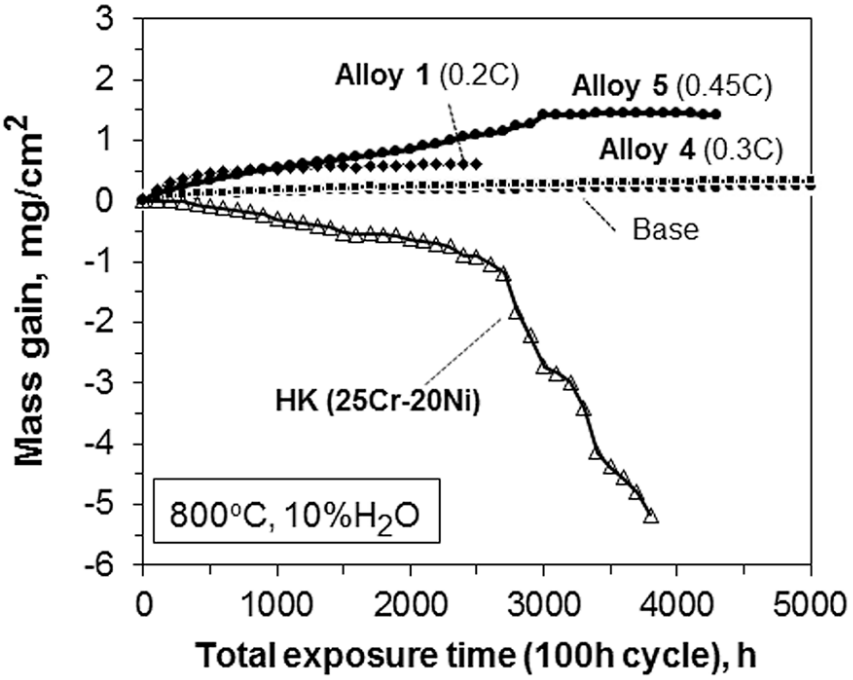

Figure 7: Oxidation results of both chromia and alumina forming alloys (10)

A major drawback of these alumina forming alloys, currently hindering their acceptance in industry, is their reduced creep resistance due to the presence of aluminum in the alloy. This poses a problem, as creep is an active mechanism at high temperatures such as those found in steam cracking plants. Therefore, alumina forming stainless steels are being researched that can compete with current chromia forming steels in mechanical properties, while outperforming in oxidation resistance (3).

1.5 Steam effects on alumina formation

Now that it is theorized that alumina forming austenitic stainless steels would outperform chromia forming alloys in corrosion resistance, there exists the issue of these steels being tested under industrial conditions. This includes the formation of alumina during the steam cleaning

process enacted to remove built up coke, and an initial pre-oxidation process prior to any usage. Currently most research into the formation of alumina involves either dry air, or air containing steam of roughly 10% by volume. This research may be useful in predicting the behavior of alumina scale under general oxidation conditions. However, pure steam environments represent the conditions present inside of the piping of a steam cracking plant during its cleaning cycle.

Experimental testing of alumina forming stainless has been conducted with varying degrees of steam purity with mixed results. It was found that under steam conditions that the alumina layer is only effected during the initial oxide formation, and does not play a role in the rest of the process. Additionally, it was found that steams presence can be detrimental under certain conditions to the formation of alumina, and can cause additional issues within the matrix (14). It is necessary to consider these findings while attempting to determine the effects of a pure steam environment.

Findings that support the benefit of steam have found that initially, the steam forces the oxidation kinetics to follow a linear trend, transitioning to a parabolic rate as the oxidation proceeds. This phenomenon is shown in Figure 8, where increasing the partial pressure of steam, *i.e.* increasing the content of steam in air, created an overall thicker oxide layer after the same time as a more dilute counterpart. In addition, the findings inferred that the steam produced a linear oxidation rate in the early stages of oxide formation, helping in the later formation of a thicker layer (15). This effect would be advantageous if applicable in pure steam, as a rapid forming oxide layer amplified by the effects of steam could possibly rival the growth rate of commercially available chromia formers.

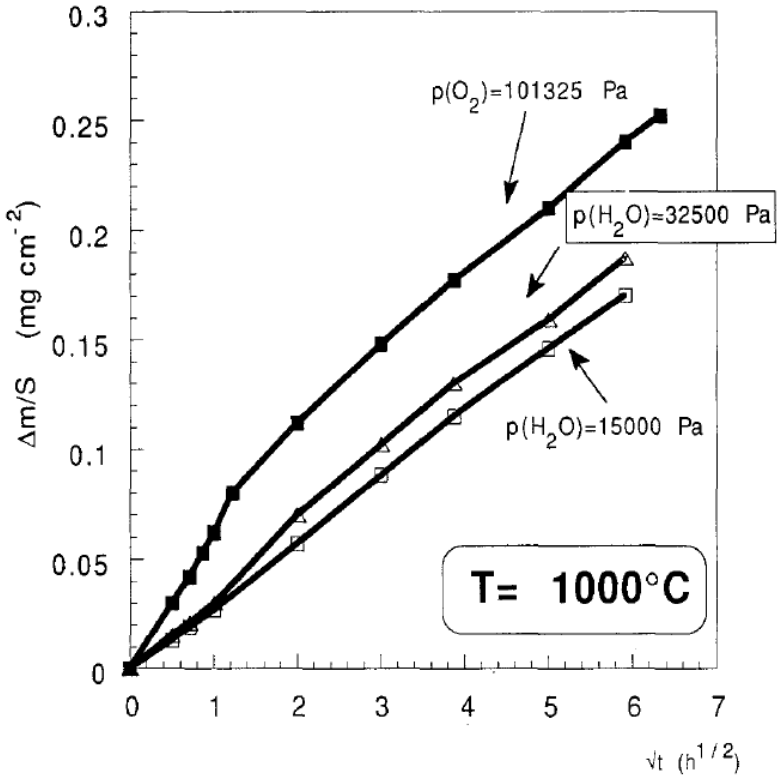

Figure 8: Alumina formation with increasing steam concentration (15)

In contrast, more recent findings state that the presence of steam has a detrimental effect on the formation of the alumina scale. These studies have found that in the presence of steam the alumina scale is not formed due to the predominance of internal oxidation. This internal oxidation prevented aluminum ions from traveling to the surface and forming the protective alumina scale. This effect can be seen in Figure 9, where samples shown in A have 3% Al and samples in B 2.5% Al. Those samples which were oxidized in air have positive specific mass gains, signifying a formed alumina scale on the surface, whereas the sample oxidized under 10% water vapor dropped to negative specific mass signifying no formation of an alumina layer (16).

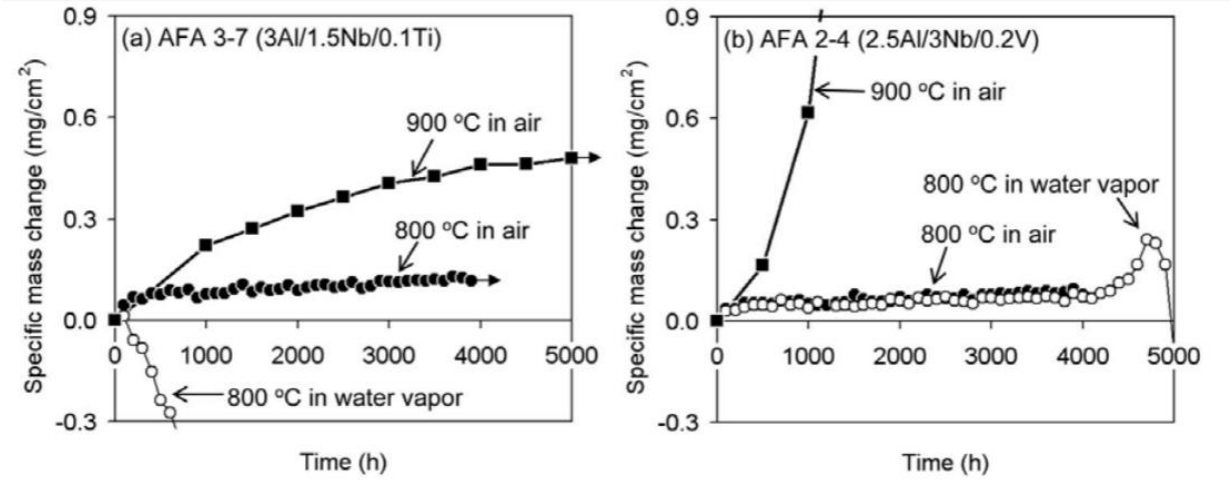

Figure 9: Detrimental effects of steam on alumina formation (16)

These studies found that the addition of other alloying elements such as niobium allowed the steel to form an alumina layer in a 10% steam environment. They proposed that this was due to the effect of niobium concentrating larger quantities of chromium in the austenitic matrix rather than forming chromium aluminum alloys on the surface. This allowed for alumina to be formed on the surface due to the third element effect. Additionally, it was theorized that the niobium allowed for the precipitation of larger quantities of B2-NiAl particles. These were found to act as holders for aluminum, and were theorized to allow for extended oxidation resistance (14).

The role of steam, and alloy content of Al in the high temperature oxidation of stainless steel alloys remains not well understood. Therefore, it is necessary to observe the interactions with a pure steam environment such as that found in steam cracking plant and the proposed alumina forming alloys. The results of which have the possibility to conform either beneficial or diminishing effects.

CHAPTER 2 – EXPERIMENTAL PROCESS

2.1 Alloy Selection

In order to determine the oxidation kinetics of new alumina forming austenitic stainless steels under pure steam conditions, samples were sectioned from four provided centrifugally as-cast pipes. These alloys were provided by MetalTek International, and were received as sections of pipe. The alloys varied in aluminum content from roughly 2.5 to 4 wt% Al which was measured by MetalTek via optical emission spectrometer. In addition, the provided alloys had similar nickel to iron ratios with several outliers.

Four alloys were chosen to represent the range of samples containing aluminum. These samples, of composition shown in Table 1, were chosen as they possess the lowest, highest, and general middle aluminum content. However, one was chosen to represent the alloys with an alternate Ni-Fe ratio shown in Table 2, while keeping the same aluminum content as another alloy. In addition, the alloy with an alternate Ni-Fe ratio was chosen due to its significantly lower content of manganese, which has shown to prevent nodule formation during oxidation (14).

Table 1: Elemental compositions of selected alloys (wt%)

Alloy	Al	C	Cr	Fe	Mn	Mo	Ni	Other
G3607-A	2.62	0.425	27.9996	26.8481	0.783	0.171	38.2575	-
G3606-A	3.2	0.43	27.5958	27.0002	0.795	0.179	37.9573	-
B3400-1	3.23	0.428	31.0537	17.2265	0.141	0.212	45.5928	-
G3610-A	3.9	0.436	27.396	24.9261	0.795	0.188	38.0119	-

*Full elemental information located in Appendix A

Table 2: Alloy ratio of nickel to iron

Alloy	Ni-Fe Ratio
G3607-A	1.4250
G3606-A	1.4058
B3400-1	2.6467
G3610-A	1.5250

2.2 Sample preparation

In order to track samples throughout the testing process each sample was given a part number which included the time, temperature, and alloy name. Additionally, each sample was assigned a roman numeral shown in Table 3 following the order they were oxidized.

Table 3: Sample designations by roman numeral

Sample	Alloy	Time (h)	Temperature (°C)
I	B3400-1	1	800
II	G3607-A	1	800
III	G3606-A	1	800
IV	G3610-A	1	800
V	B3400-2	1	950
VI	G3607-A	1	950
VII	G3606-A	1	950
VIII	G3610-A	1	950
IX	B3400-3	30	800
X	G3607-A	30	800
XI	G3606-A	30	800
XII	G3610-A	30	800
XIII	B3400-4	30	950
IXV	G3607-A	30	950
XV	G3606-A	30	950
XVI	G3610-A	30	950
XVII	B3400-5	3	950
XVIII	G3607-A	3	950
XIV	G3606-A	3	950
XX	G3610-A	3	950
XXI	B3400-6	3	800
XXII	G3607-A	3	800
XXIII	G3606-A	3	800
XXIV	G3610-A	3	800
XXV	B3400-7	10	800
XXVI	G3607-A	10	800
XXVII	G3606-A	10	800
XXVIII	G3610-A	10	800
XXIX	B3400-8	10	950
XXX	G3607-A	10	950
XXXI	G3606-A	10	950
XXXII	G3610-A	10	950

Samples were prepared from as-cast pipe sections, and were cut down with an abrasive saw to pieces of roughly the same dimensions per Figure 10 with the original inner and outer diameters being unknown. Variables X_1 and X_2 represent the inner and outer diameters. Following this the samples were ground using silicon carbide to 600 grit, with all sides except the ID being processed. This was due to the fact that the ID of the pipe was machined during manufacturing. Because of this machining it was felt that grinding them would result in less accurate results, and were therefore left untouched.

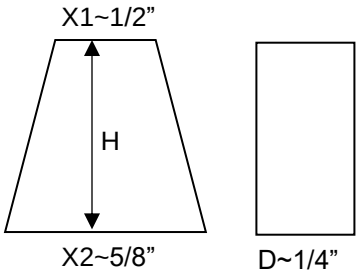

Figure 10: Rough dimensions of samples after cutting

2.3 Testing apparatus

The goal of these tests was to produce an oxidation environment of pure steam. This being the key requirement of the experiment made it necessary to remove air and any other gasses inside of the testing apparatus. This was done by using a steam pot, and an inert gas purge system shown in Figure 11.

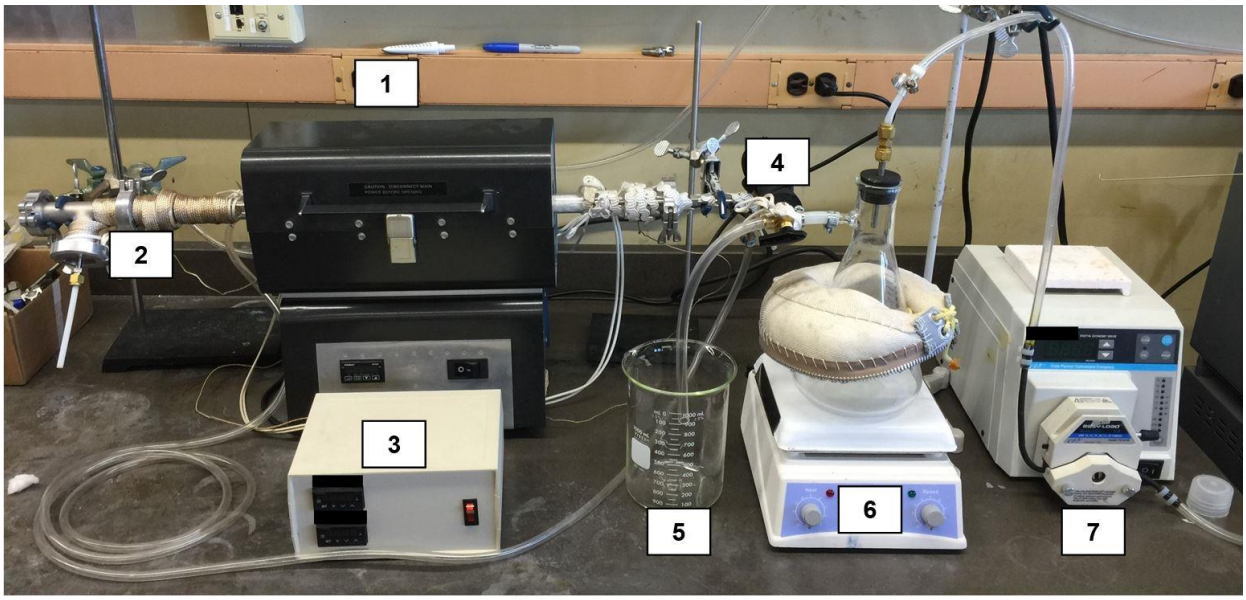

Figure 11: Oxidation apparatus

Features of the testing setup in include:

1. Split tube furnace with quartz 1” tube, and programmable temperature controller
2. Heated steam exit vent and sample loading access
3. Heated inlet and exit regulation unit
4. Three-way heated inlet valve for nitrogen/steam change and three-way valve for steam to furnace/atmosphere
5. Steam overflow vent during nitrogen use
6. Hot plate with magnetic stir bar
7. Peristaltic pump for water replenishment

The apparatus was designed so that temperatures of up to 1000 °C can be obtained in the furnace, while steam is constantly flowed throughout the chamber. The process in which to obtain an environment of pure steam includes the purging of the system with nitrogen prior to switching to steam flow, and then having the steam bottle sealed from the atmosphere. This allows only steam

to vent through the chamber while the flow rate of steam is held at sufficient levels to ensure that back flow was not possible, eventually purging the system of anything but steam.

2.4 Oxidation Schedules

For the steel to oxidize it was necessary to develop oxidation schedules. It was determined that four time increments would develop a sufficient oxidation profile. Therefore, the times that were selected for investigation were 1, 3, 10, and 30 hour trials. These were selected because each time increment is roughly three times larger than the previous and would create a better spacing of data when analyzed in a semi-logarithmic fashion. An example of the 1 hour oxidation profile is shown in Figure 12 and shows that the overall time required for a run at 950 °C is larger than that of an 800 °C run. This is due to the maintained increase in temperature that was chosen of 10 °C per minute.

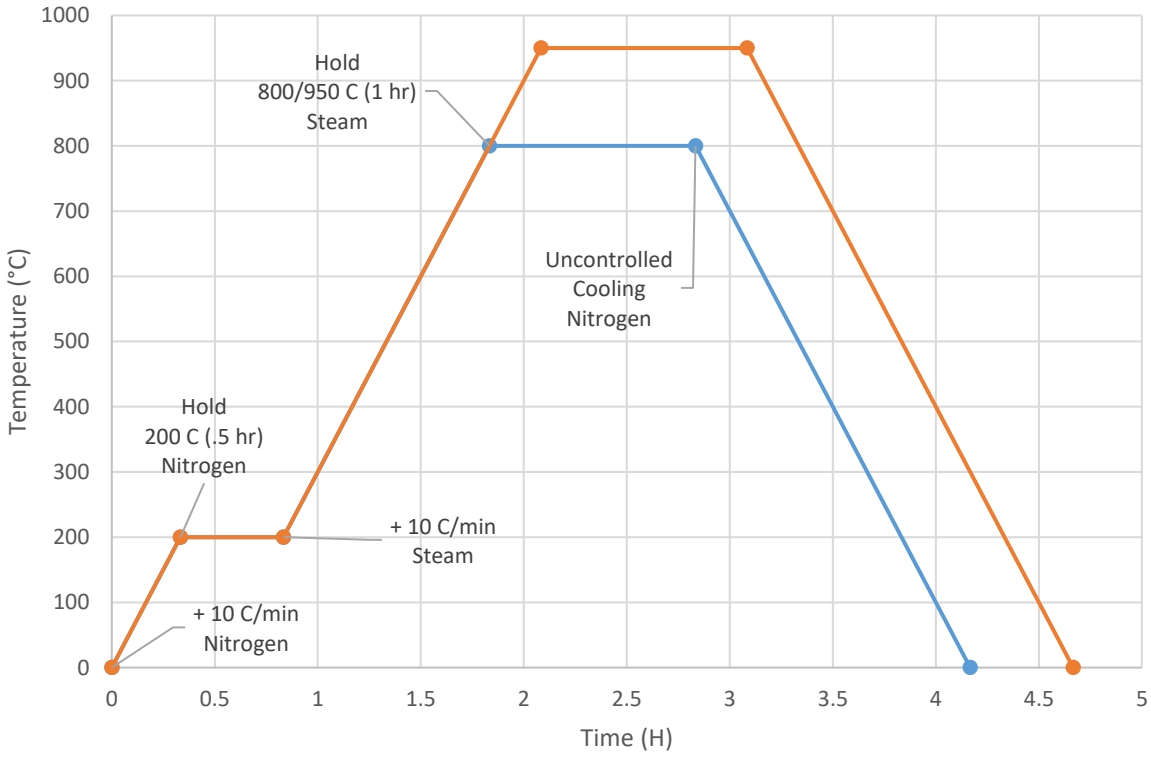

Figure 12: Oxidation schedule example for 1 hour

The oxidation profiles were designed so that the steel samples were first heated and stabilized at 200 °C while the chamber was being purged with nitrogen. This allowed for the system to start at an environment that could be replicated from run to run while allowing for steam to be generated. Following the stabilization and purge, the system was switched to steam while the furnace was ramped up to the final hold temperature of either 800 °C or 950 °C. Following the completion of the oxidation hold period, the system was shut off, and the steam was purged from the chamber with nitrogen as samples were cooled. Cooling rates varied from 5 to 30 °C per minute depending on ambient temperature and gas flow of nitrogen during cooldown.

2.5 Pre-testing measurements

Prior to any oxidation run a batch of samples was subjected to pre-oxidation measurements. Each sample was assumed to take the generic shape of a trapezoidal prism as shown in Figure 10, this resulted in the neglect of curvature from ID and OD. Each sample was measured for its mass, and dimensions of which are tabulated in Table 5 and Table 4. Each sample had its surface area calculated via Equation 5, and is expressed along with each sample's dimensions in Table 5.

$$SA = D\left[\left(X_1 + X_2 + 2\sqrt{H^2 + \frac{1}{4}(X_2 - X_1)^2}\right) + [X_1 + X_2]\right] \quad \textit{Equation 5}$$

Where SA is surface area, D is depth, X_1 and X_2 are the horizontal measurements for ID and OD width, and H is height all shown in Figure 10

Table 4: Sample dimensions and calculated surface area

	DIMENSION (mm)				
SAMPLE	X_1	X_2	H	D	SA (mm^2)
I	12.70	17.13	11.52	6.97	579.36
II	11.86	15.72	12.20	6.31	503.94
III	10.68	15.02	12.36	6.45	493.41
IV	13.29	15.42	11.79	6.23	505.23
V	12.41	16.75	11.42	7.00	570.98
VI	12.27	14.61	12.38	5.83	458.41
VII	11.33	14.02	12.51	6.19	469.60
VIII	11.75	13.81	12.03	5.85	440.32
IX	11.72	16.80	12.63	6.47	535.75
X	12.32	14.92	12.37	6.20	492.01
XI	12.30	15.30	12.72	6.62	535.00
XII	11.80	15.85	11.70	6.63	524.09
XIII	12.46	16.11	12.66	6.58	544.31
IXV	13.79	15.42	12.25	6.34	526.06
XV	11.55	14.16	12.80	6.12	472.17
XVI	12.53	15.16	11.90	5.84	463.26
XVII	11.99	16.67	12.43	6.42	530.40
XVIII	12.14	14.80	12.57	6.91	547.00
XIV	13.26	13.75	13.01	6.41	513.09
XX	13.19	14.37	12.06	6.66	527.93
XXI	12.44	16.44	12.60	7.41	617.07
XXII	12.64	14.43	12.26	6.28	494.39
XXIII	15.49	15.34	12.78	6.10	532.04
XXIV	11.71	14.60	11.91	6.80	520.98
XXV	13.14	16.18	12.09	6.75	560.32
XXVI	13.11	15.86	12.36	5.92	490.25
XXVII	12.57	14.94	12.76	6.26	504.87
XXVIII	11.06	14.85	11.79	6.63	501.91
XXIX	12.97	16.28	12.38	7.01	585.20
XXX	12.81	15.35	12.57	6.30	514.00
XXXI	12.12	14.50	12.99	6.51	516.43
XXXII	12.64	12.70	12.21	7.09	532.46

Table 5: Mass of samples measured pre oxidation treatment

SAMPLE		G3607-A (2.6%)	G3606-A (3.2%)	B3400-1 (3.23%)	G3610-A (3.9%)
TEMP (°C)	TIME (h)	Initial Mass (g)			
800	1	8.43780	8.21795	9.7121	7.957958
	3	7.92450	8.5128	10.0318	8.0144
	10	8.13458	8.24127	8.83286	7.59748
	30	8.11498	8.90497	9.066	7.9326
950	1	7.43134	7.57874	9.877	6.68437
	3	8.47600	8.2366	8.8707	8.15
	10	8.33975	8.13714	9.37459	8.11327
	30	8.70885	7.55823	6.6854	7.22331

2.6 Characterization

2.6.1 Optical Stereography

Samples were observed post oxidation using a Zeiss Stemi 2000-C optical stereoscope for physical changes. This allowed for the observance of any physical appearance changes, such as color or visible microstructure. In addition, this process allowed for the sub classification of samples based on resulting physical changes.

2.6.2 Raman Spectroscopy

Samples were analyzed on the ID using a Renishaw 1000 Micro Raman spectroscope in order to determine the refractive peaks associated with potential oxide layers developed during the oxidation process. A laser of 633 nm, grating of 1800 I/mm, and a focal lens of 50X was used in the collection of peak data.

2.6.3 Scanning Electron Microscopy (SEM)

High magnification images of developed oxide layers were taken with a Hitachi S-4800 scanning electron microscope in order to determine the continuity of the layer. Images were taken using an accelerating voltage of 15 keV. This was done to maintain a standard in which to measure the thickness of the oxide layer.

2.6.4 Energy Dispersive Spectroscopy (EDS)

In order to measure accurately the thickness of any developed oxide layer a method other than change in mass was utilized. The Bruker EDS attached to the Hitachi S-4800 was determined to be the most reliable method short of mass change in measuring oxide layer thickness due to its ability of detecting variations in elemental composition. Prior to EDS samples were bisected through the ID and OD according to Figure 13 using a diamond abrasive saw, mounted in conductive Bakelite, and polished.

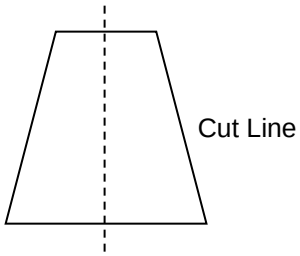

Figure 13: Method of bisection before mounting and EDS analysis

Samples were then analyzed using a 1 micrometer scanning range at 50,000X with 200 points of measurement in said line scan. This method allowed for the analysis of elemental composition every 5 nanometers. In the case of an oxide layer being greater than the standard scanning range of 1 micrometer, the magnification was to be decreased to 25,000X and a scan range of 2 micrometers with 400 points was to be used. This method allowed for the keeping of a 5

nanometer resolution. Each EDS scan was to track elemental data for the elements Fe, Cr, Ni, Al, and O as this allowed for interpretation of the beginning of the oxide layer, any elemental mixtures, and the base metal.

2.6.5 X-Ray Diffraction

X-Ray diffraction was performed on samples following one hour oxidation. Diffraction results yielded inconclusive data. This was due to low intensities resulting from thin oxide layers. Further XRD testing was not performed. Because XRD was deemed ineffective in determining resultant oxide layer, Raman spectroscopy was substituted as the preferred method of layer characterization.

CHAPTER 3 – EXPERIMENTAL RESULTS

3.1 Changes in mass

The standard method to identifying oxidation kinetics is through the change in mass of a sample. Therefore, each sample had its initial mass recorded and then was again measured following the oxidation process. The final mass of each sample is recorded in Table 6, with the change in mass over the oxidation process calculated in Table 7.

Table 6: Mass of samples measured post oxidation

SAMPLE:		G3607-A (2.6%)	G3606-A (3.2%)	B3400-1 (3.23%)	G3610-A (3.9%)
TEMP (°C)	TIME (h)	Final Mass (g)			
800	1	8.43952	8.21698	9.71226	7.95677
	3	7.92510	8.5137	10.0323	8.015
	10	8.13470	8.24155	8.83299	7.59779
	30	8.11434	8.90503	9.06644	7.9331
950	1	7.43051	7.5812	9.87728	6.68745
	3	8.48121	8.238	8.8718	8.1513
	10	8.34112	8.13931	9.37565	8.11568
	30	8.70891	7.559125	6.68821	7.22521

Table 7: Overall change in masses of samples during oxidation

SAMPLE:		G3607-A (2.6%)	G3606-A (3.2%)	B3400-1 (3.23%)	G3610-A (3.9%)
TEMP (°C)	TIME (h)	ΔMass (g)			
800	1	0.00172	-0.00097	0.00016	-0.00119
	3	0.00060	0.00090	0.00050	0.00060
	10	0.00012	0.00028	0.00013	0.00031
	30	-0.00064	0.00006	0.00044	0.00050
950	1	-0.00083	0.00246	0.00028	0.00308
	3	0.00521	0.00140	0.00110	0.00130
	10	0.00137	0.00217	0.00106	0.00241
	30	0.00006	0.00089	0.00281	0.00190

Additionally, the change in mass for each sample is shown graphically in Figure 14 and Figure 15 filtered by the temperature at which the samples were oxidized.

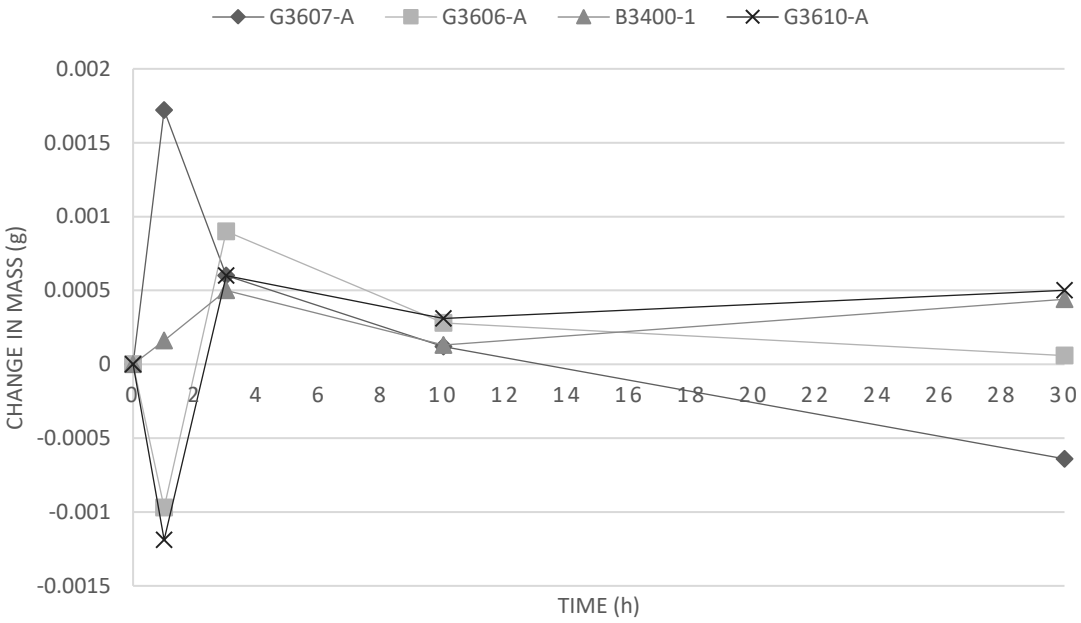

Figure 14: Change in mass of samples at 800 °C

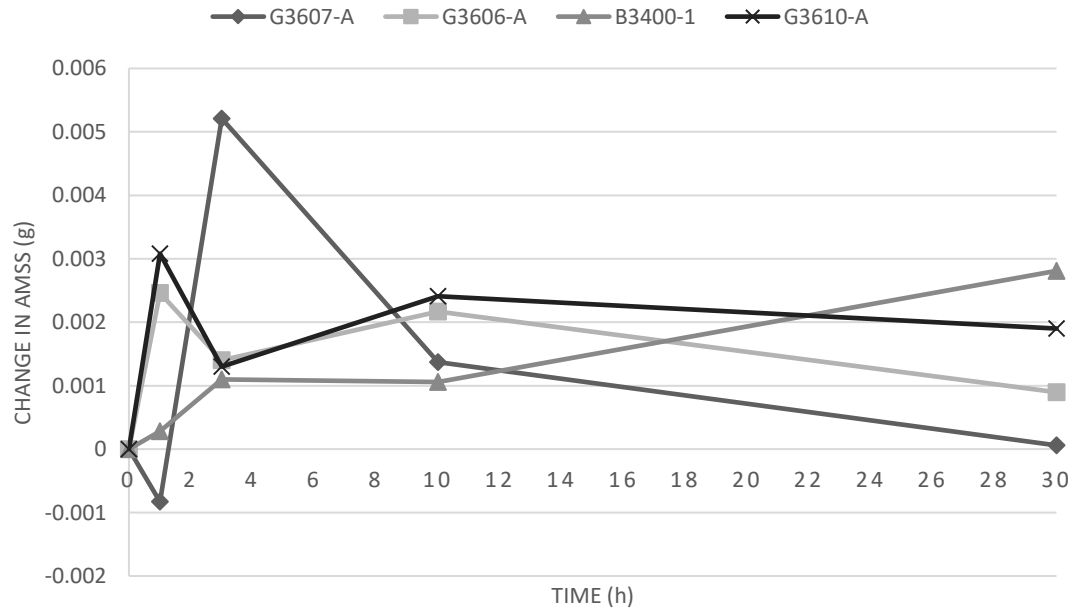

Figure 15: Change in mass of samples at 950 °C

It can be seen that the change in mass for several samples is negative. This would indicate that a sample had not developed an oxide layer, and rather corroded during the oxidation run. However, in comparing the samples with negative mass to those of positive mass in the same time bracket, the data is inconsistent and is therefore being considered inconclusive.

3.2 Optical stereoscope results

All samples were observed for physical changes post oxidation using a Zeiss Stemi 2000-C optical stereoscope. A color change from the original metal was observed in samples oxidized at 800 °C versus those oxidized at 950 °C. Samples that were exposed to 800 °C developed a blue coloration to all surfaces, while samples exposed to 950 °C developed a grey and rainbow coloration on all surfaces. This phenomenon can be seen from Figure 16 to Figure 17 where samples of G3607-A were oxidized for 3 hours at 800 °C and 950 °C and photographed at 25X on the trapezoidal face. Besides the color change of samples, no discernable physical changes were observed in any of the samples.

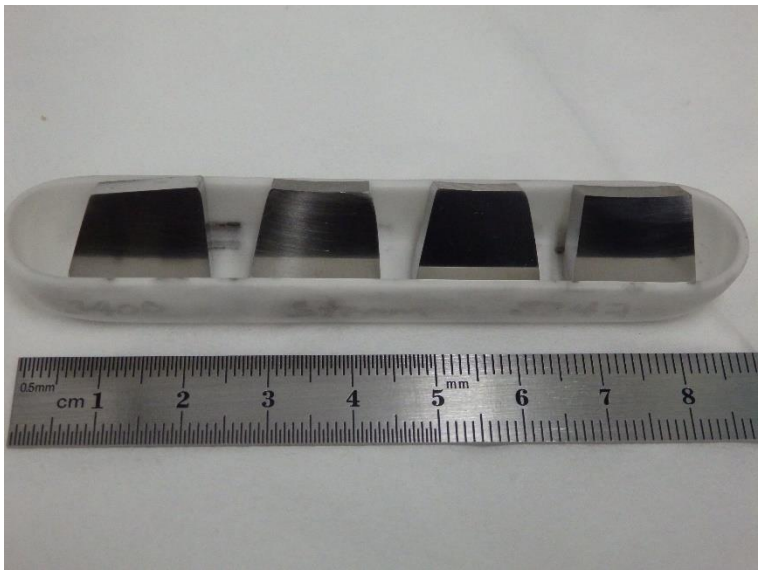

Figure 16: Polished Samples prior to oxidation

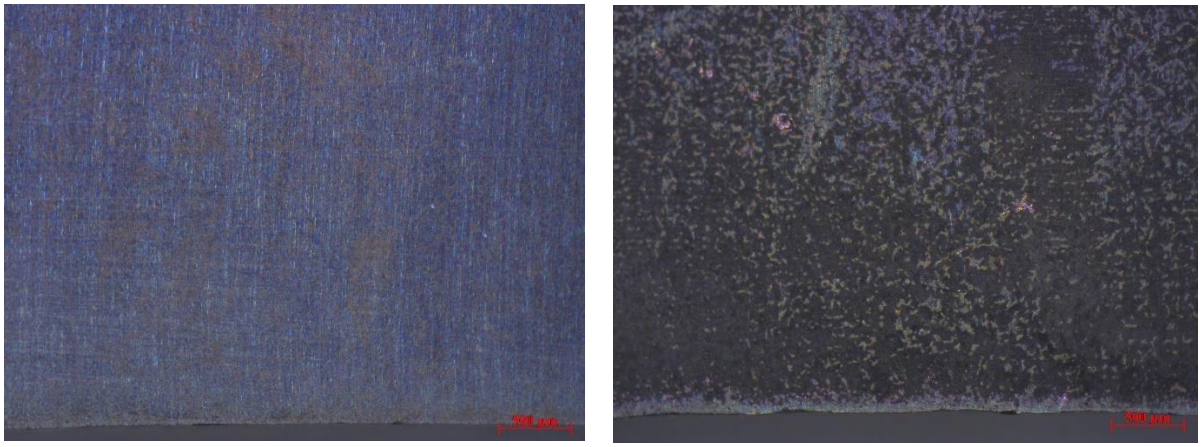

Figure 17: Color Changes of G3607-A (2.6%) after 3 hours at 800 °C (left) & 950 °C (right) 500 µm scale

3.3 Raman spectroscopy

Each sample was examined with Raman spectroscopy, in order to determine the type of oxide layer developed during the oxidation process. In order to complete this, a raw sample of each alloy was taken and analyzed to lay a baseline of the samples before oxidation. It was expected, due to the nature of Raman spectroscopy that the bare metal surface would result in no peaks as no oxide should be present. This was proven to be true in Figure 18, and shows that prior to oxidation the metals had no observable oxide layer (17).

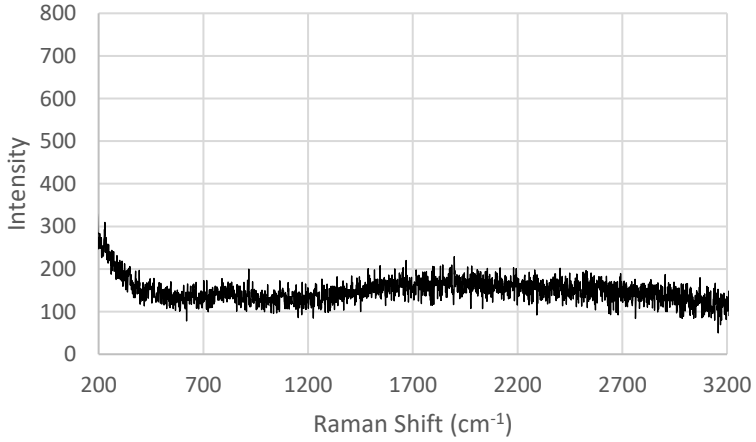

Figure 18: Example of raw metal G3610-A Raman spectrum

As the samples were proven to be free of oxide prior to processing, a control was taken in order to compare the developed oxide layer. The material tested as a control sample was 99.5% pure α-alumina powder. The resulting Raman spectra can be seen in Figure 19, and shows a single double tipped peak at 1370.3 and 1399.8 cm^{-1}. This information was used to determine if an oxide was in fact alumina after processing.

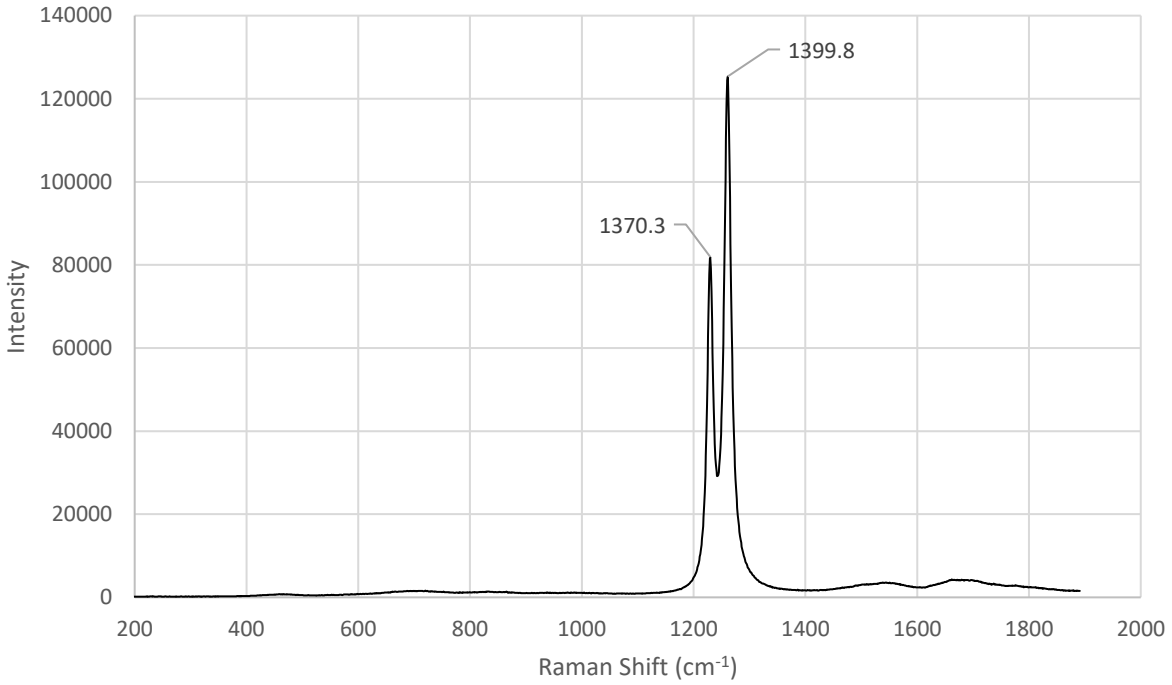

Figure 19: Raman Spectra of 99.5% α-alumina powder

In addition to alumina power it was considered that there was the possibility of a chromium oxide layer forming on samples. In order to investigate this a sample of 99.9% chromium (III) oxide was examined using Raman. The Raman spectrum for chromia is shown in Figure 20, and shows several peaks that have low intensity ranging from 100 to 600 cm^{-1}. The full range for this spectrum was severely affected by background interference, only showing discernable peaks in this range.

Each sample was scanned with Raman and produced various peaks. The spectrums that were produced all resulted in roughly one to three peaks, of which sample VII shown in Figure 21 has all three. Other samples spectrums resulted in only one or two peaks of which are tabulated in

Table 8.

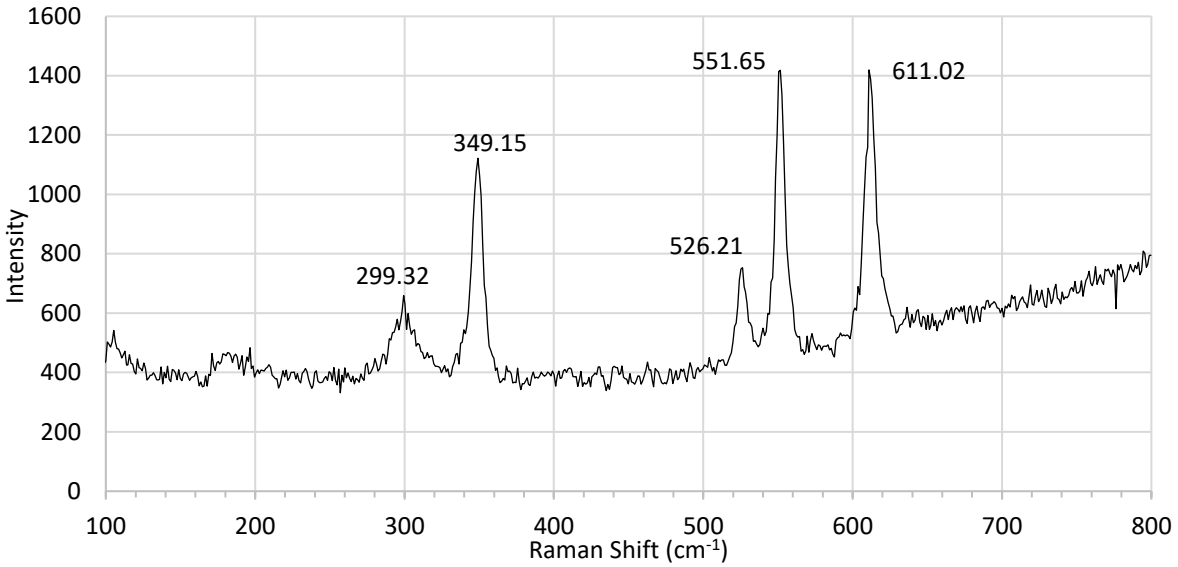

Figure 20: Raman Spectra of 99.9% chromium (III) oxide

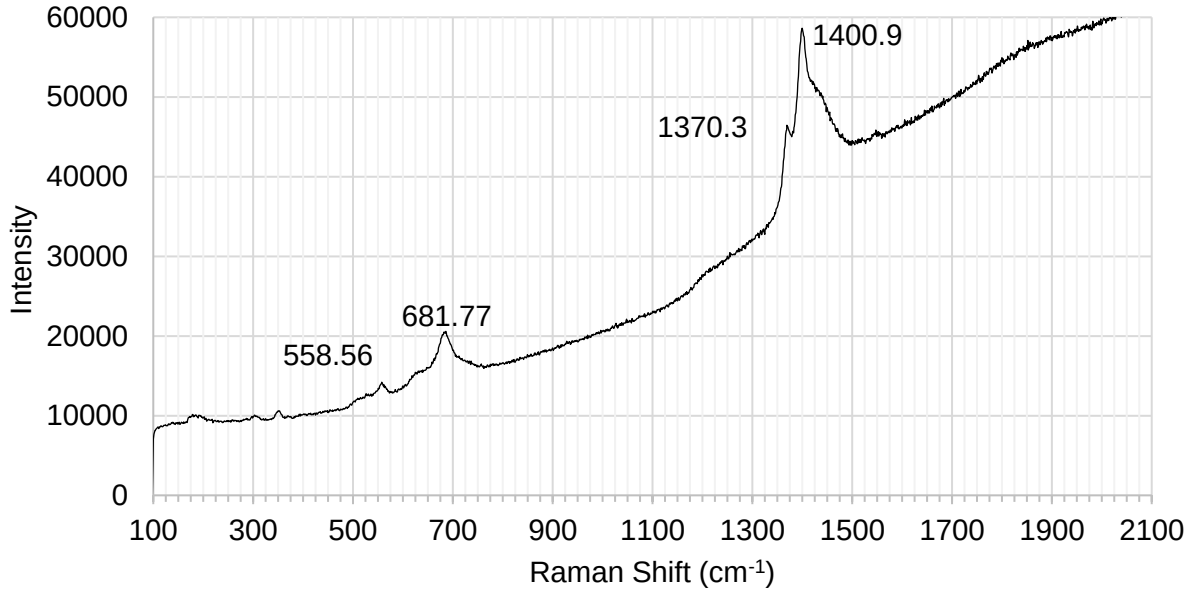

Figure 21: Raman spectrum of sample VII (G3606-A-1H-950C-VII)

Table 8: Raman peaks for each sample

	Raman Shift [cm^{-1}]		
Sample	Peak 1	Peak 2	Peak 3
Alumina	1370.30	1399.80	-
Chromia	349.15	551.65	611.02
I	705.40	1435.00	-
II	693.13	1426.30	-
III	692.26	1427.20	-
IV	700.13	1420.20	-
V	685.63	1387.80	1417.50
VI	693.52	1393.10	1421.90
VII	686.14	1369.50	1399.20
VIII	1371.20	1400.90	-
IX	688.01	1440.40	-
X	681.89	1422.00	-
XI	1375.70	1407.20	-
XII	1374.80	1407.40	-
XIII	1372.20	1401.90	-
IXV	693.50	1425.50	-
XV	712.48	1384.40	1413.30
XVI	701.99	1381.80	1408.90
XVII	688.01	1432.50	-
XVIII	679.27	1395.80	1424.60
XIV	683.64	1423.80	-
XX	713.35	1431.60	-
XXI	707.24	1415.30	1625.30
XXII	705.49	1403.70	1627.40
XXIII	712.48	1413.30	-
XXIV	1419.40	-	-
XXV	705.49	1435.10	-
XXVI	685.39	1438.60	-
XXVII	1426.40	-	-
XXVIII	695.10	1418.50	1852.80
XXIX	1431.60	-	-
XXX	631.21	1395.80	1424.60
XXXI	629.46	1391.40	1420.30
XXXII	620.72	1389.70	1422.90

3.4 SEM results

Each sample's ID was examined using SEM to determine if a visible layer was formed on the metal surface. An example of the progression of oxide development over the range of testing times is shown in Figure 22 and Figure 23. It can be seen that as time progresses the oxide layer becomes thicker, requiring images to be taken at 25,000X instead of the standard 50,000X.

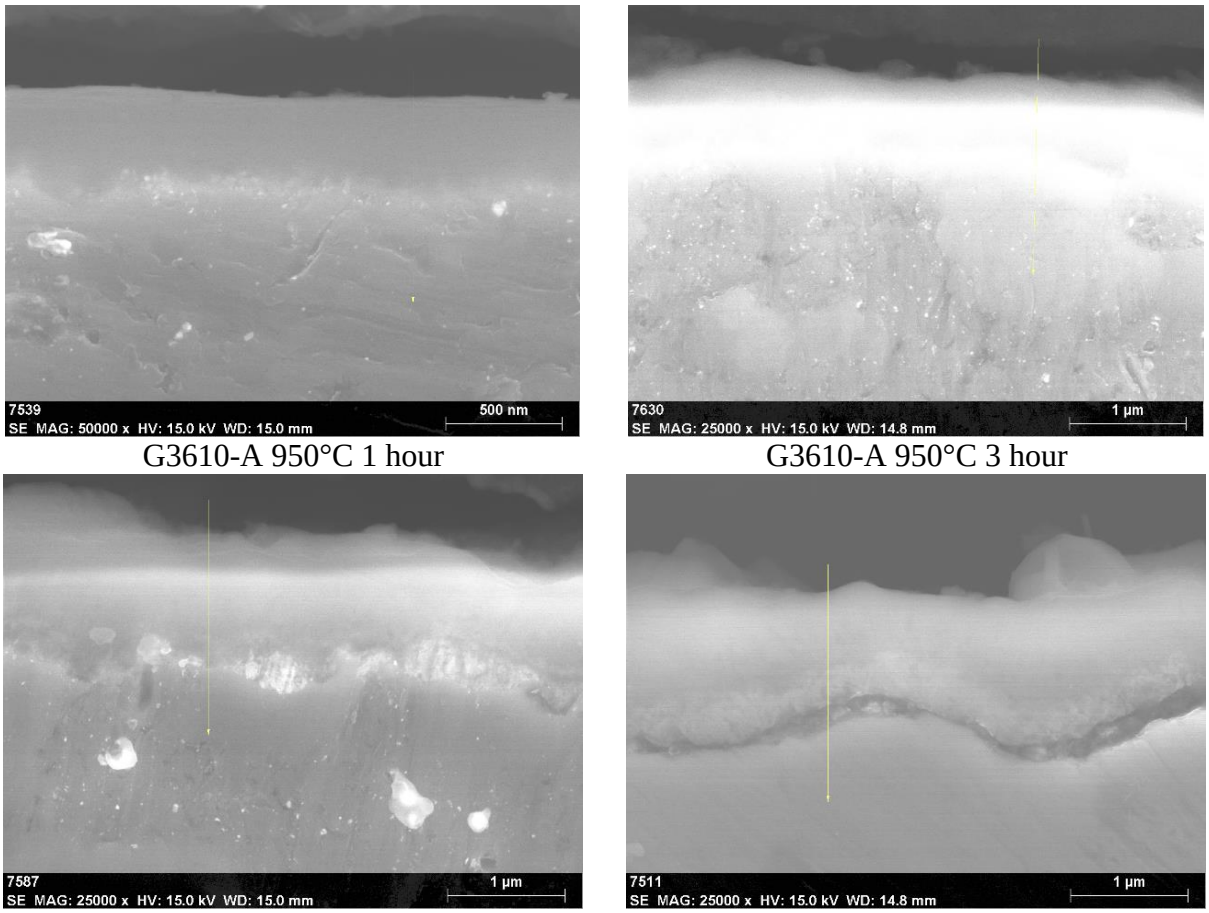

G3610-A 950°C 1 hour

G3610-A 950°C 3 hour

G3610-A 950°C 10 hour

G3610-A 950°C 30 hour

Figure 22: SEM of G3610-A (3.9%) at 950°C at each time interval

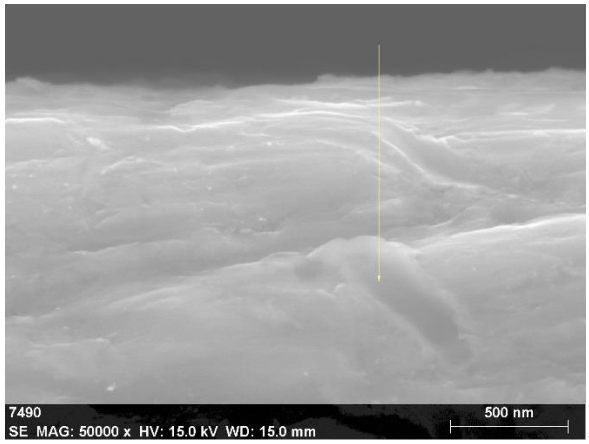

G3610-A 800°C 1 hour

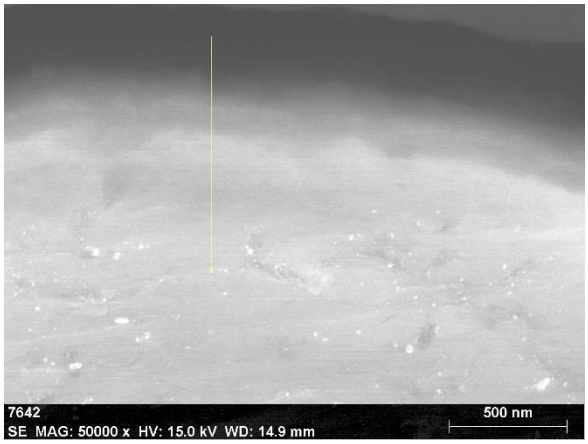

G3610-A 800°C 3 hour

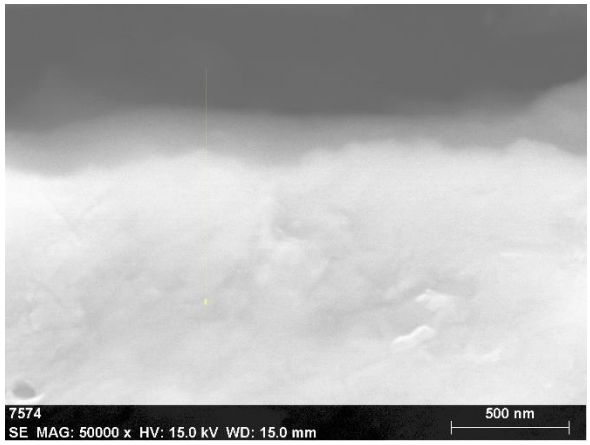

G3610-A 800°C 10 hour

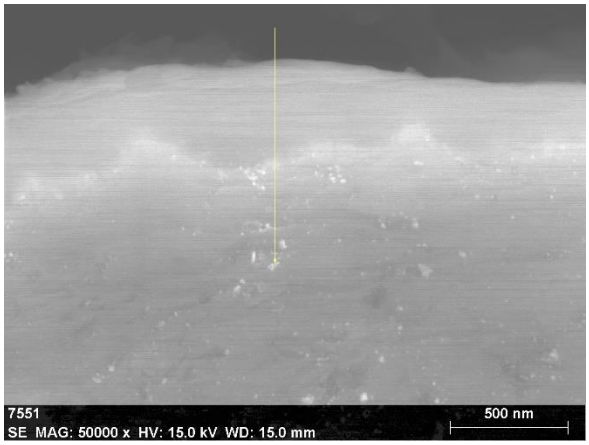

G3610-A°C 30 hour

Figure 23: SEM of G3610-A (3.9%) at 800°C at each time interval

In addition to the observed oxidation of the ID, it was observed in Figure 24 that internal oxidation of the metal had occurred on the OD of the samples treated at 950 °C. This phenomena was not observed on any of the 800 °C samples nor on any of the IDs.

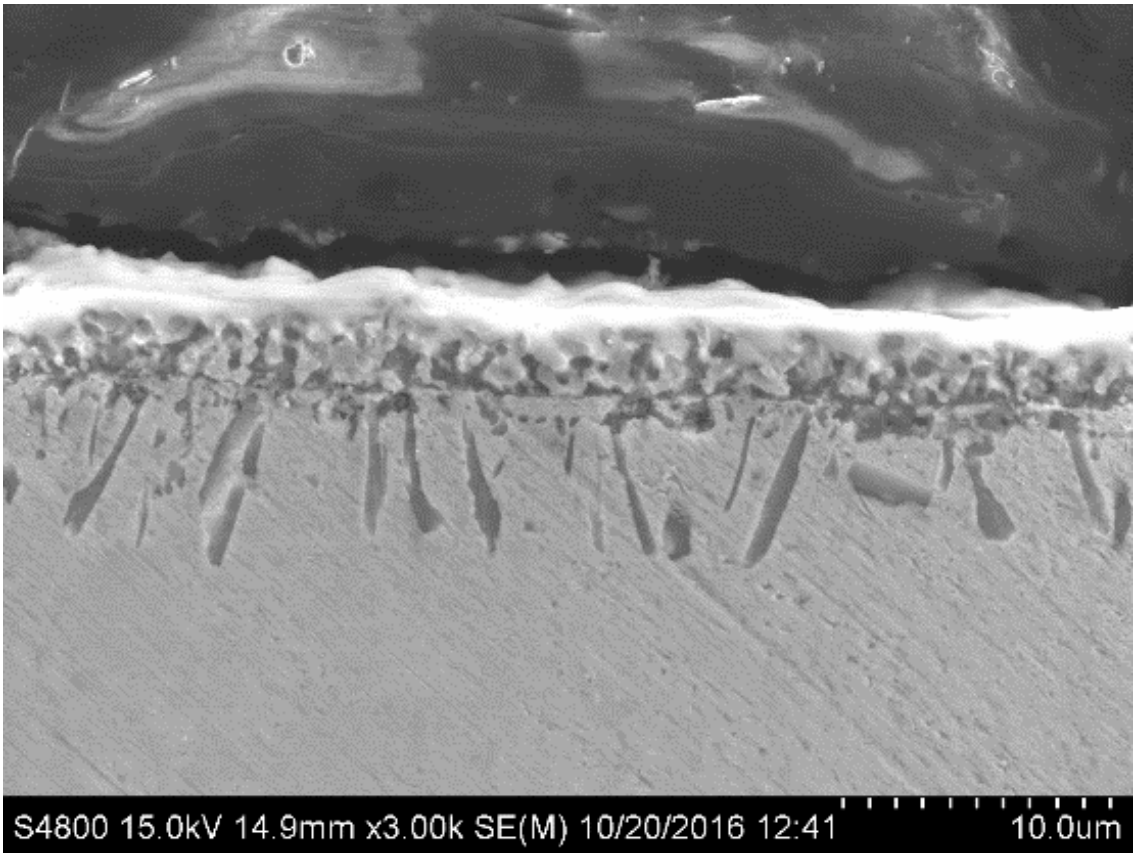

Figure 24: Internal oxidation of alloy in 950 °C samples

3.5 EDS oxide thickness measurements

It was initially thought that the oxide layer could be quantified by mass measurements. However, results were inconclusive, and unfortunately it was not possible to directly measure oxide thickness through means such as SEM. This was due to edge charging resulting from an aversion to plating samples post oxidation. From other work, it was seen that when oxidized samples were electroplated with copper, polishing produced an undesirable effect in which the oxide layer was dislodged from the surface of the metal. Therefore, samples were not plated but mounted as oxidized. As SEM was not able to directly observe the oxide layer thickness, EDS was used to measure the elemental composition of the oxide layer, and then to quantify any thickness measurements by changes in elemental composition. Two to three EDS scans were performed on each sample ID in various locations separated by distances larger than one

millimeter. This was done in order develop a value for average oxide layer thickness. Scans were performed from the mounting material into the bulk of the metal, perpendicular to the surface. Readings were presented as reports which included line scans as shown in Figure 25 across the oxide layer from the mounting material into the bulk of the sample. These reports were automatically generated by the Bruker software and an example can be seen in Appendix B.

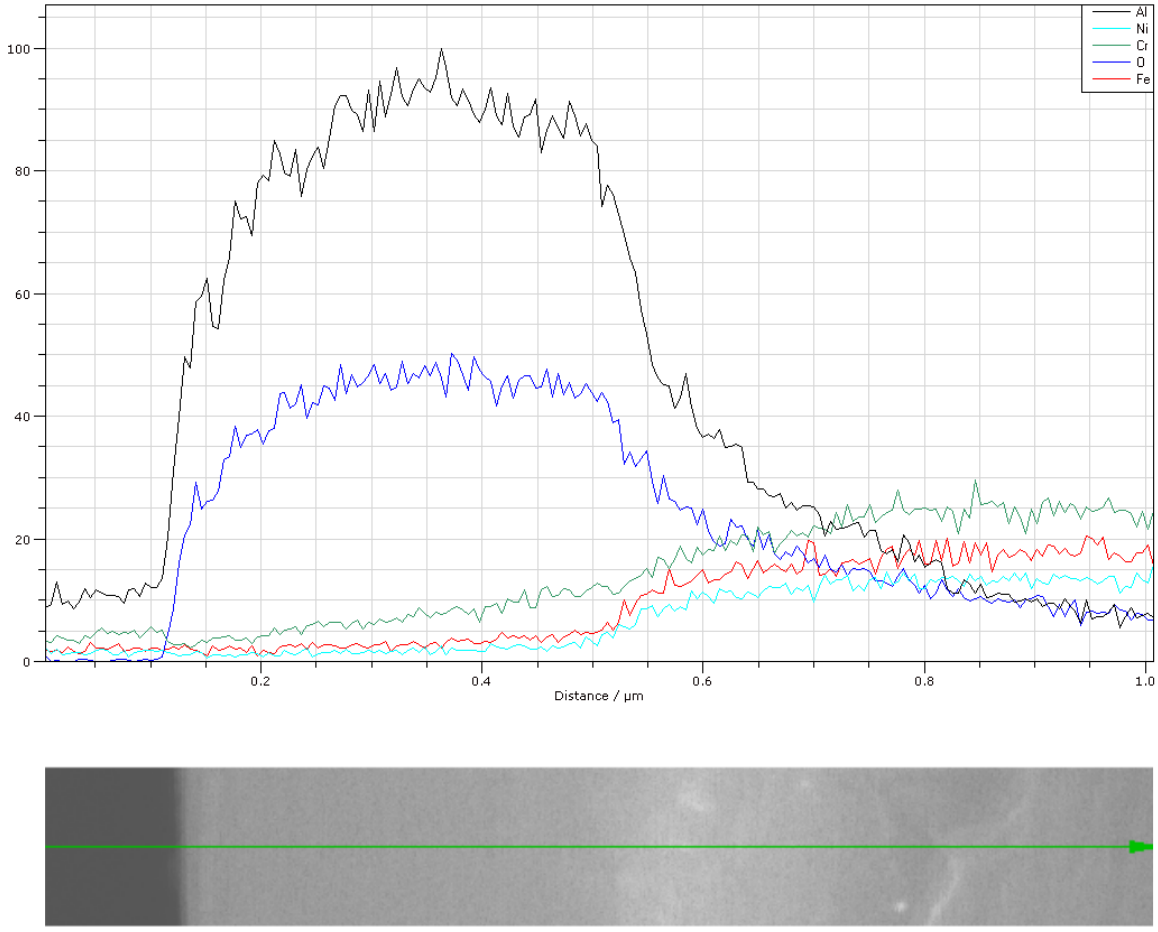

Figure 25: Sample EDS scan of G3610-A-950C-1H

From each line scan a measurement was taken of oxide layer thickness, based upon various considerations. These considerations effected the start and end locations of where the oxide was believed to exist. The reasoning for this was to account for data that showed the presence of aluminum or oxygen before the edge of the sample was considered to be present.

Likewise, the oxide layer was deemed to terminate when either aluminum or oxygen crossed the chromium line. This was considered to be the location in which aluminum oxide ceased to exist as a relatively pure oxide, and began to form mixtures with the base metal and chromium oxide.

From each sample the average thickness in Table 9 of the oxide layer was determined for each time and temperature tested, with all measurements available in Appendix C

Table 9: Average alumina thickness results

		Average Thickness (μm)			
Temp. (°C)	Time (h)	G3607-A (2.6%)	G3606-A (3.2%)	B3400-1 (3.23%)	G3610-A (3.9%)
800	1	0.188	0.163	0.125	0.163
	3	0.108	0.175	0.283	0.288
	10	0.325	0.242	0.150	0.238
	30	0.338	0.338	0.142	0.567
Temp. (°C)	Time (h)	G3607-A (2.6%)	G3606-A (3.2%)	B3400-1 (3.23%)	G3610-A (3.9%)
950	1	0.388	0.600	0.288	0.438
	3	0.400	0.525	0.258	1.017
	10	0.550	0.667	0.375	1.175
	30	0.838	0.833	0.333	1.300

The average oxide thickness for each sample is shown graphically in Figure 26 through Figure 29

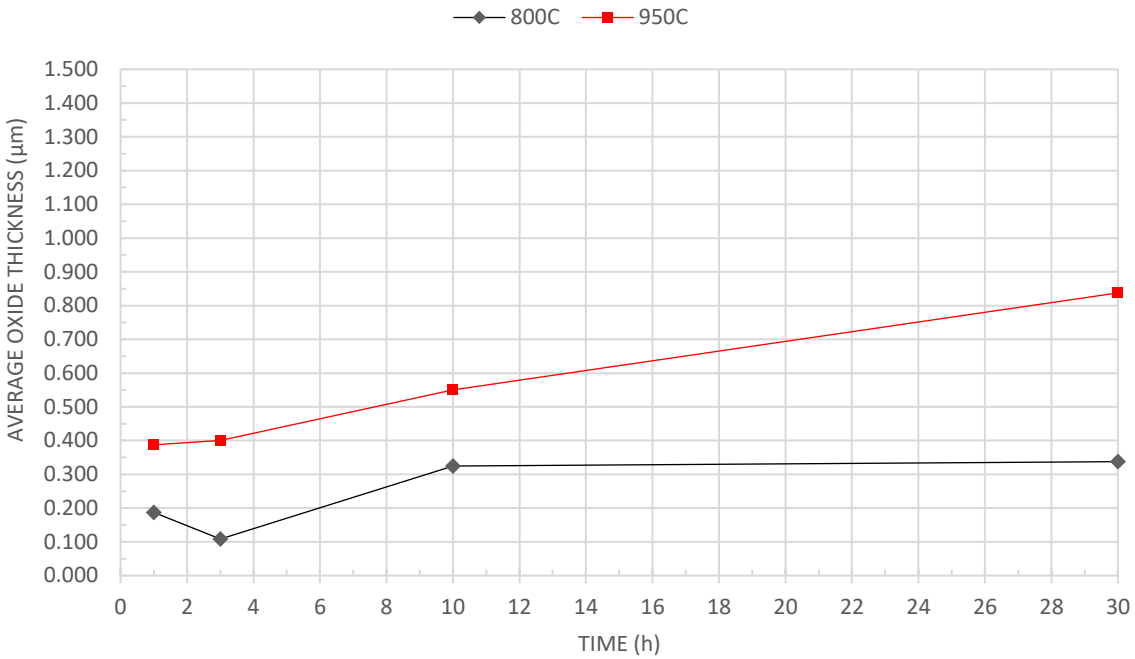

Figure 26: Oxide layer thickness result of G3607-A (2.6%)

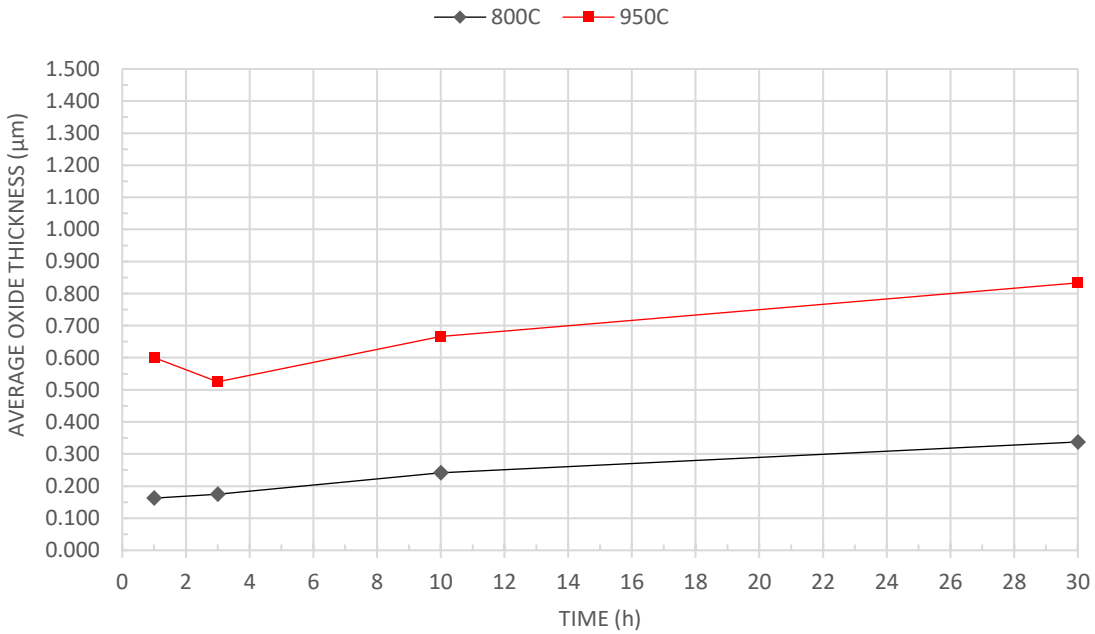

Figure 27: Oxide layer thickness result of G3606-A (3.2%)

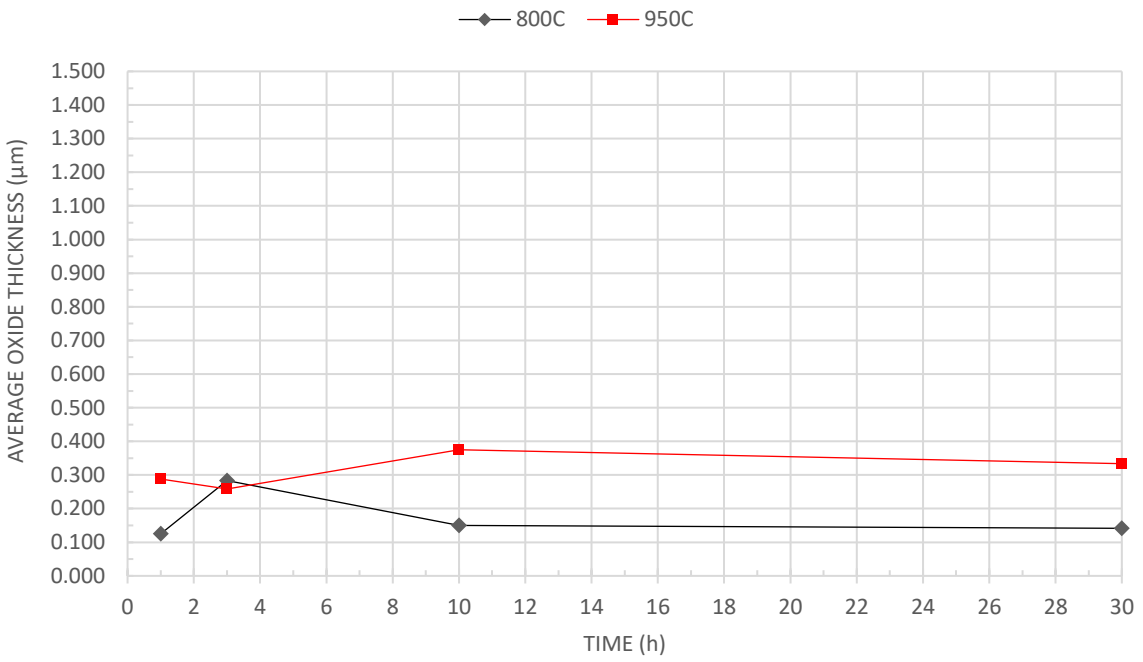

Figure 28: Oxide layer thickness result of B3400-1 (3.23%)

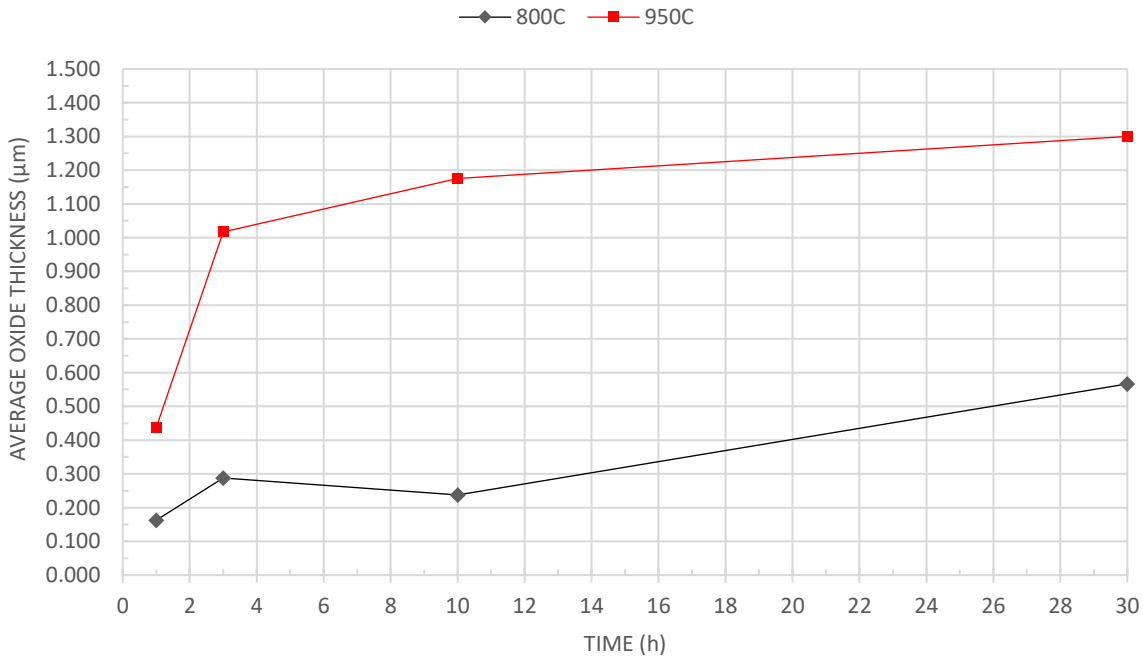

Figure 29: Oxide layer thickness result of G3610-A (3.9%)

CHAPTER 4 – ANALYSIS & DISCUSSION

4.1 Wagner rate constant

In order to determine the parabolic rate constant for each alloy and temperature the average thickness of oxide developed was plotted as a function of square root of time. This would follow Wagner's model, and force the data to fit a parabolic nature. Therefore, each alloys data was analyzed and is shown in Figure 30 through Figure 33. On each plot, a linear trend line was added in order to determine the value of *kp* from the slope. The trend lines were forced to a intercept of zero, regardless of fit to replicate ideal conditions of no oxide being present on the metal at time zero. Each of these values was then tabulated in Table 10 for further analysis.

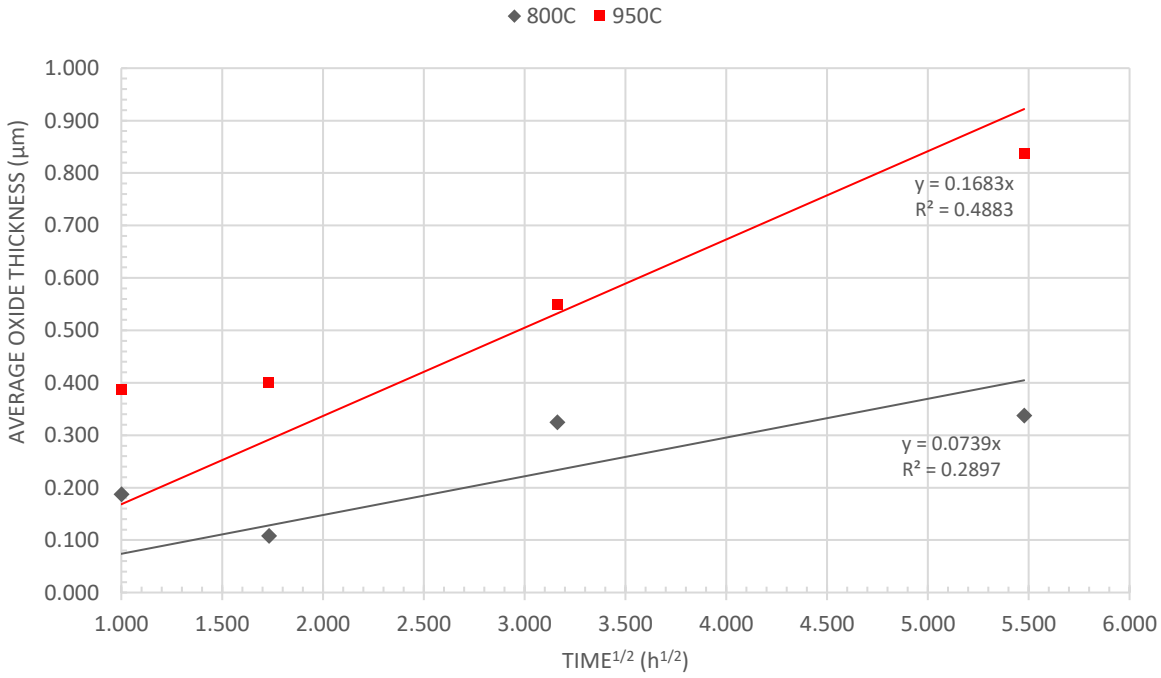

Figure 30: kp value of G3607-A (2.6%) determined by forcing Wagner model

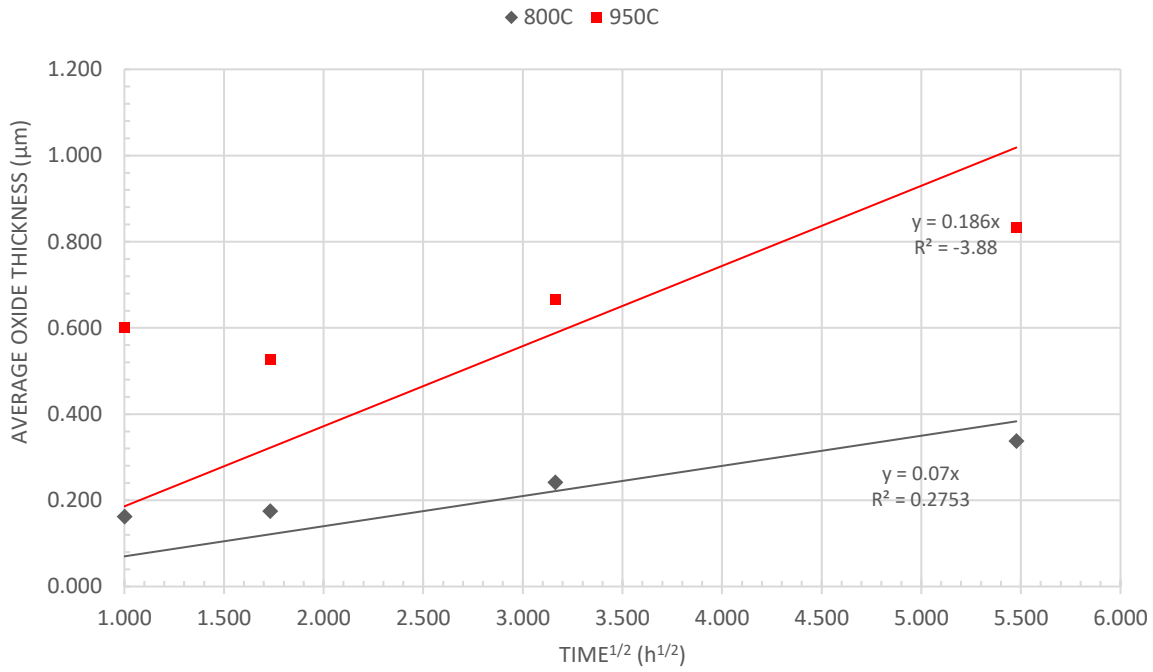

Figure 31: kp value of G3606-A (3.2%) determined by forcing Wagner model

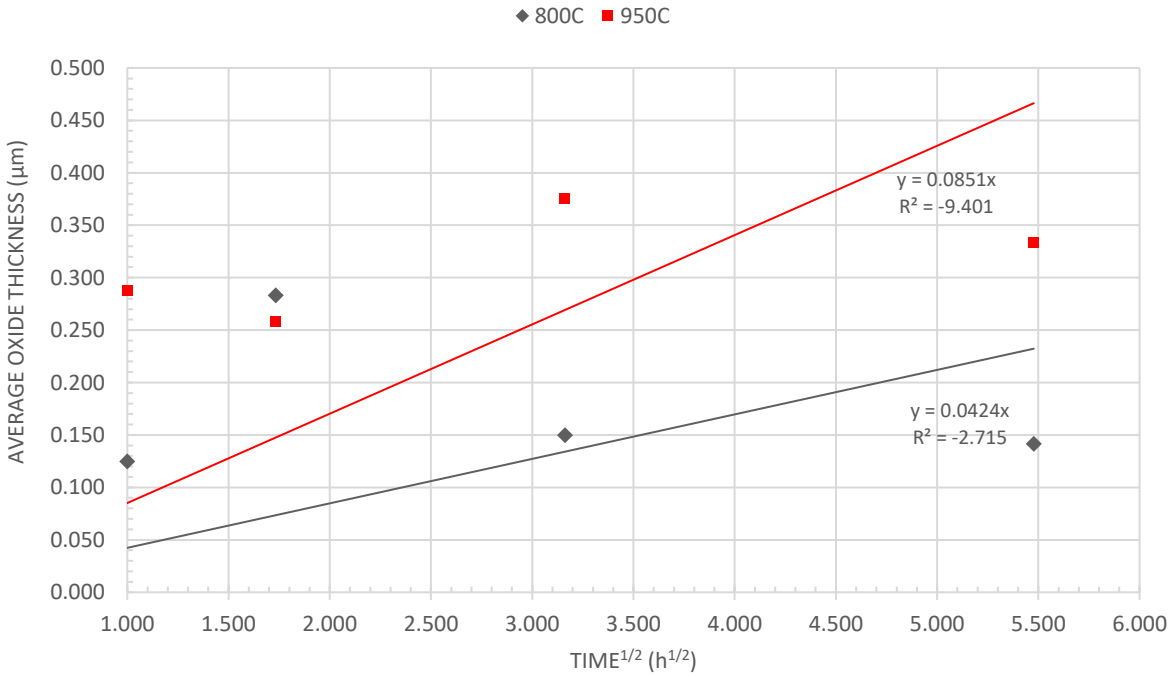

Figure 32: kp value of B3400-1(3.23%) determined by forcing Wagner model

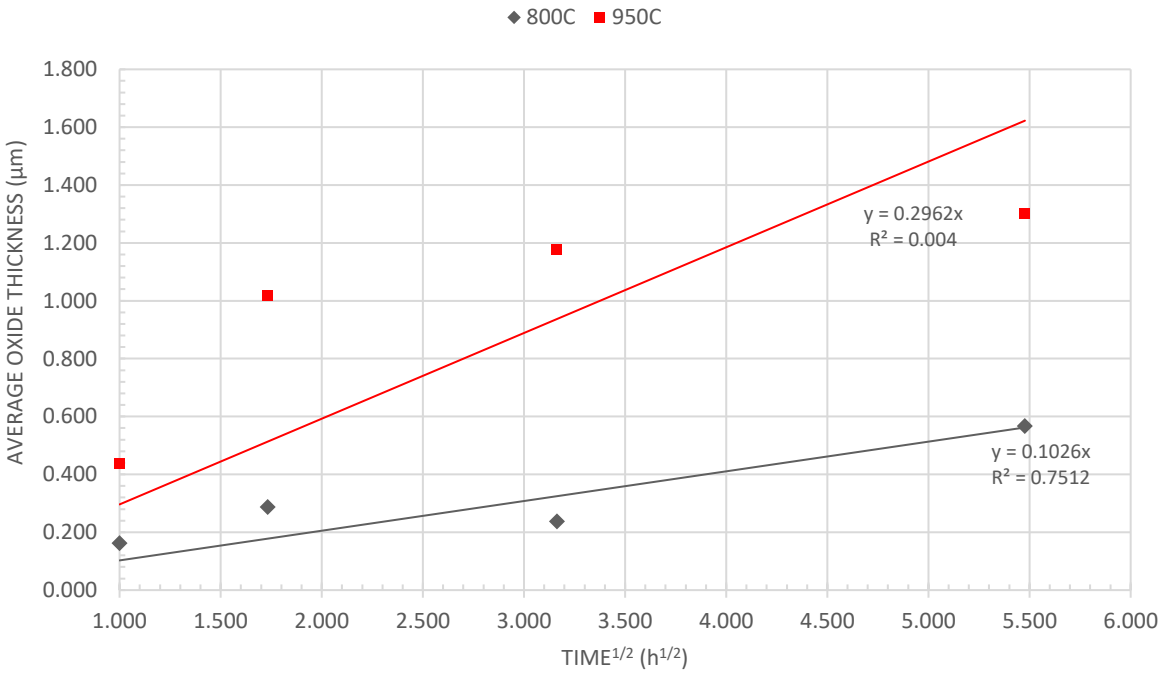

Figure 33: kp value of G3610-A (3.9%) determined by forcing Wagner model

Table 10: Forced parabolic rate constants for all alloys

Kp [µm/s$^{1/2}$]	Temperature [°C]	G3607-A (2.6%)	G3606-A (3.2%)	B3400-1 (3.23%)	G3610-A (3.9%)
n=1/2	800	0.045	0.041	0.004	0.081
	950	0.105	0.062	0.016	0.160

However, after observing the R^2 values for each of the linear trend lines generated, it was deemed necessary to compare the raw data to an idealized plot of what data would appear as if plotted. Therefore, each *kp* was taken and compared to it respective raw data with an example shown in Figure 34. From these plots it was observed that the *kp* values should be further investigated as they appear to follow a parabolic trend as time increases, however in the very start the data begins to deviate from the theoretical curve.

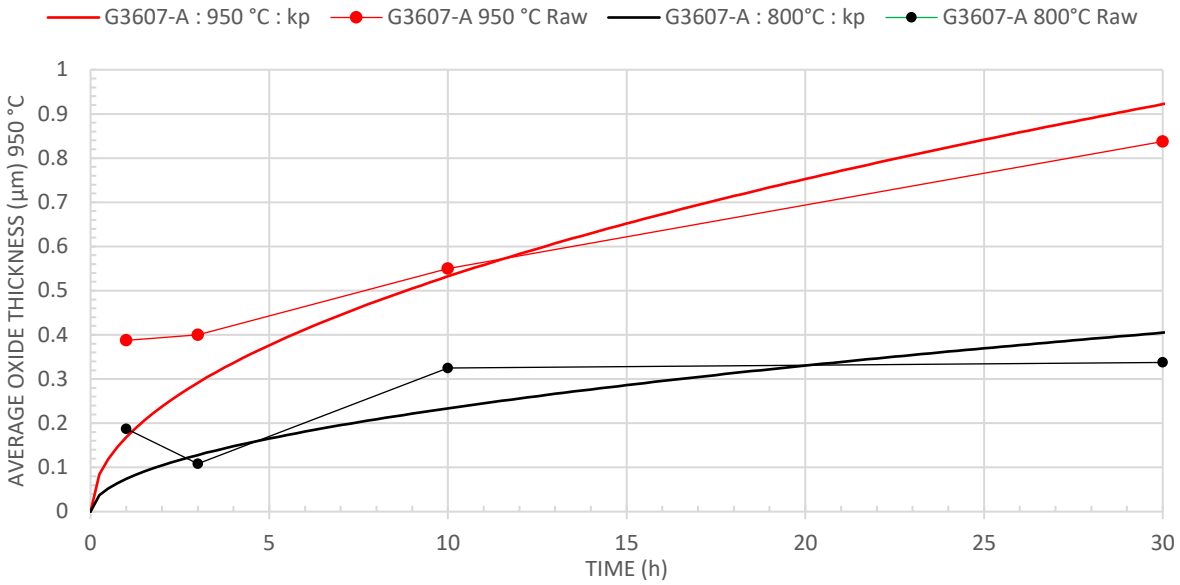

Figure 34: Comparison of theoretical kp lines to raw data of G3607-A (2.6%)

In order to identify if an experimentally determined rate constant would provide a more accurate model to base results upon, plots using equation 4 were created.

4.2 Modifications to Wagner rate constant

As it was determined that the Wagner model did not fit data to a satisfactory level of accuracy, an analysis of the *n* value and ln(*kn)* for each set of data was performed. In order to do this the natural log was taken of the parabolic rate law in order to solve for *n* and *ln(kn)* as the slope and intercept of the regression, respectively. Each alloy for both temperatures developed a different *n* value and *kn* of which can be seen in **Error! Reference source not found.**. These were determined in the same manner as each *kp* value where the slope of a linear trend line through the data was used to calculate the experimental values. The plots used to find each *n* and ln(*kn)* value are shown in Figure 35 through Figure 38.

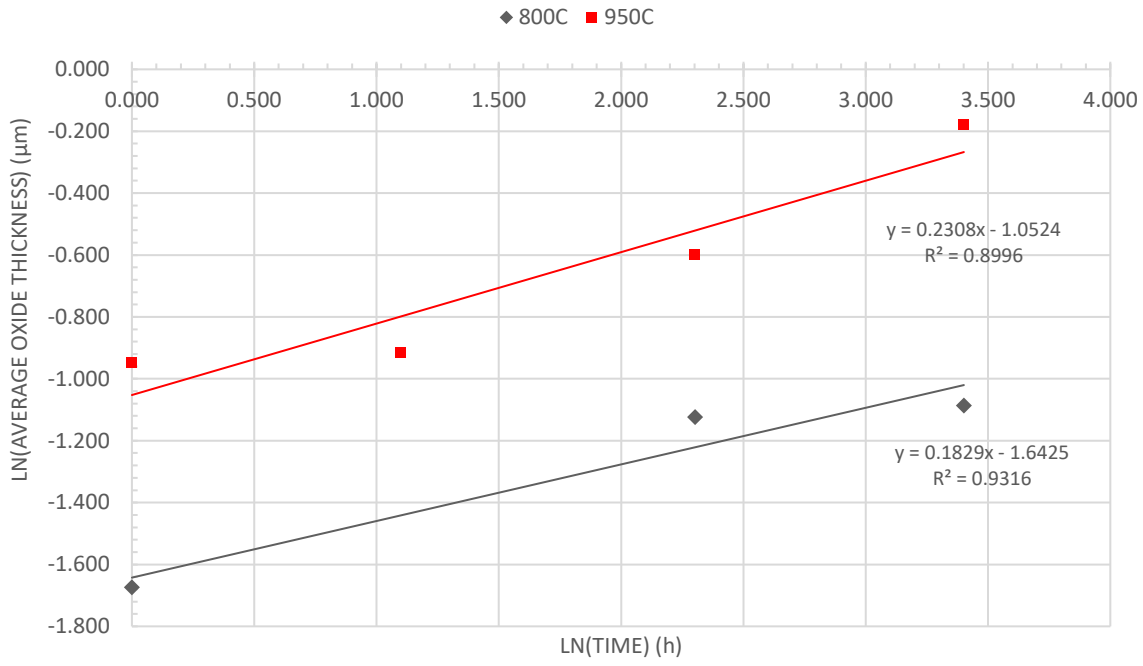

Figure 35: Analysis of n value for G3607-A (2.6%)

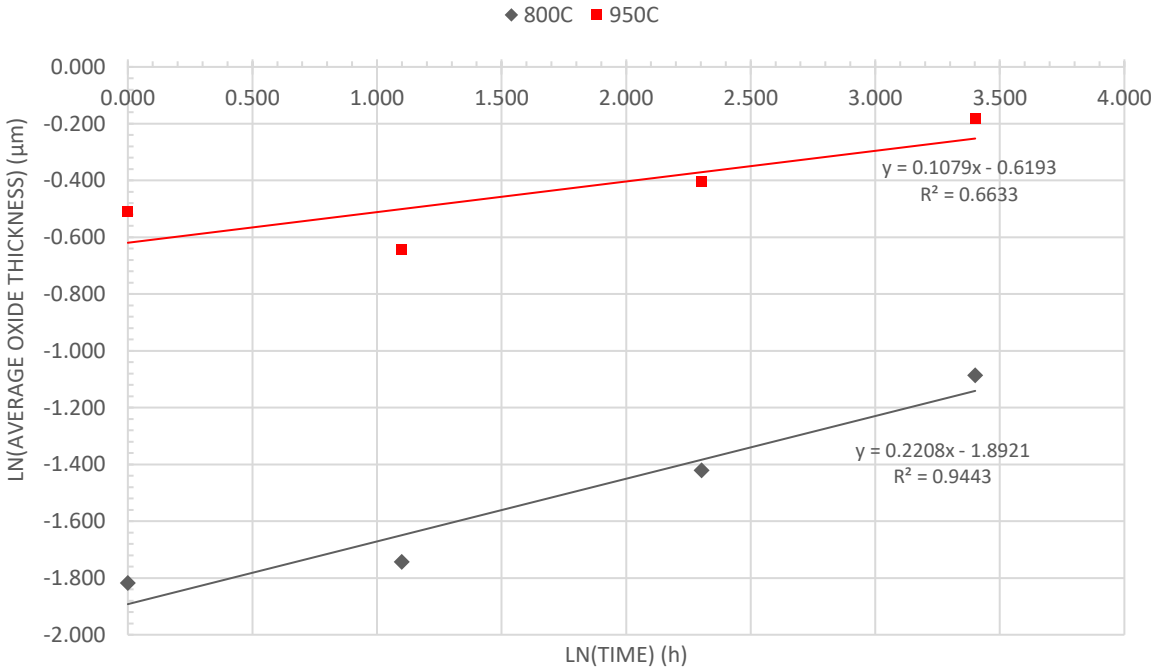

Figure 36: Analysis of n value for G3606-A (3.2%)

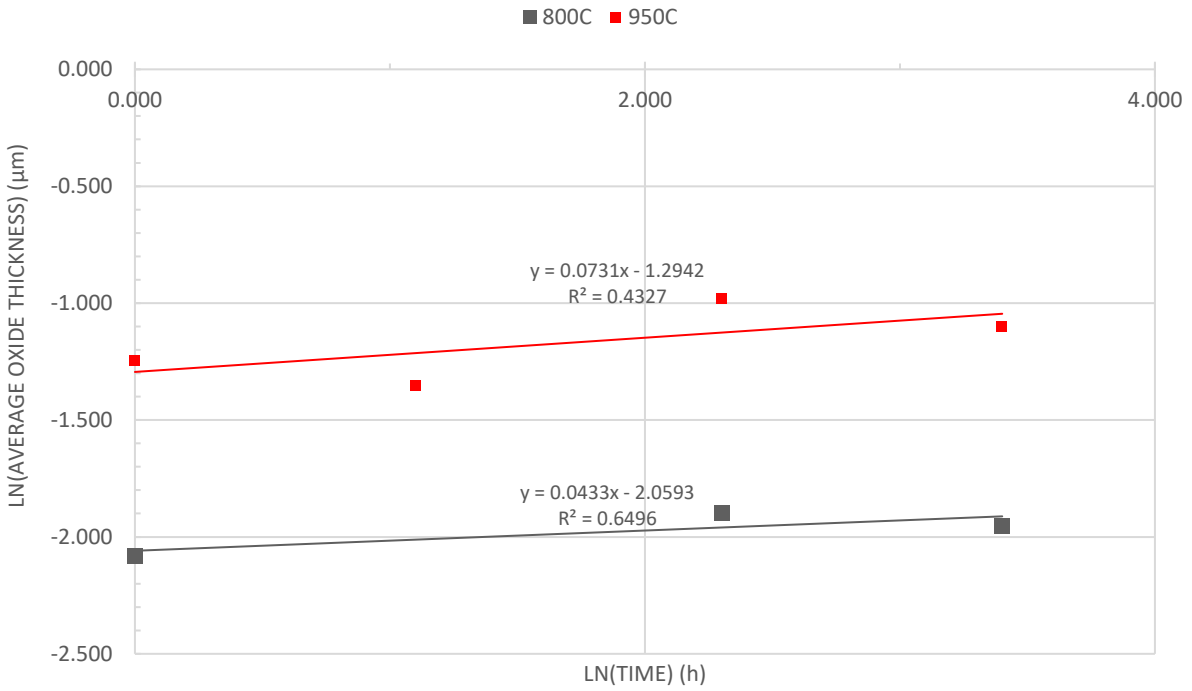

Figure 37: Analysis of n value for B3400-1 (3.23%)

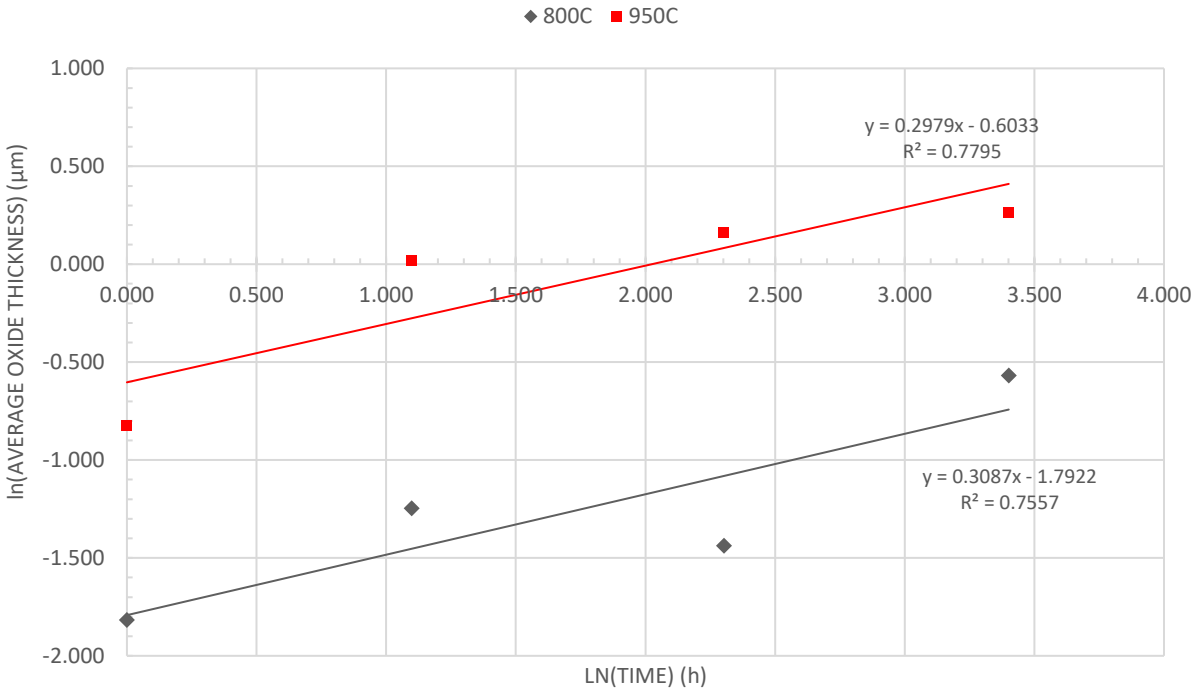

Figure 38: Analysis of n value for G3610-A (3.9%)

After the value for each alloys *n* and *ln(kn)* value was calculated, the experimental *n* rate constant, *kn* was calculated.

Table 11: Calculated experimental kn values

Temperature [°C]	Variable	G3607-A (2.6%)	G3606-A (3.2%)	B3400-1 (3.23%)	G3610-A (3.9%)
800	n	0.183	0.221	0.043	0.309
	kn [µm/h^n]	0.193	0.151	0.128	0.167
950	n	0.231	0.108	0.073	0.298
	kn [µm/h^n]	0.349	0.538	0.274	0.547

In order to establish any trends in the values of *kp*, *n*, and *kn*, with respect to the aluminum content in samples, histograms of each value were created shown in Figure 39 through Figure 41.

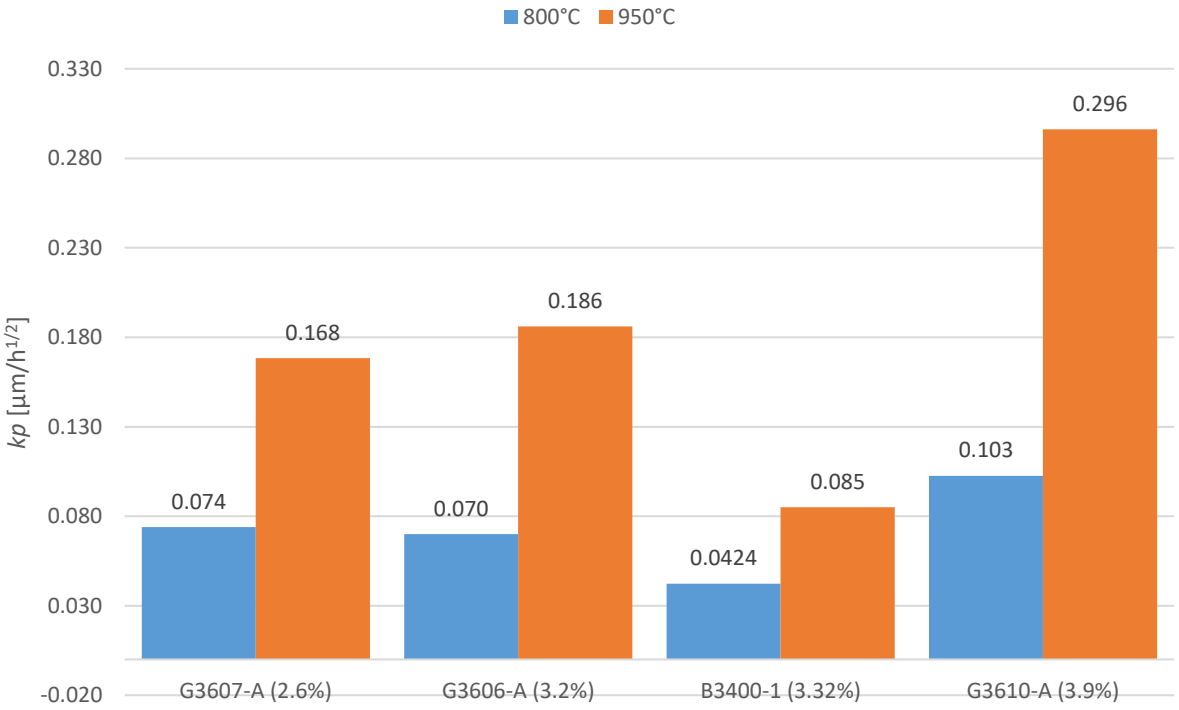

Figure 39: Histogram of kp values as a function of wt% Al

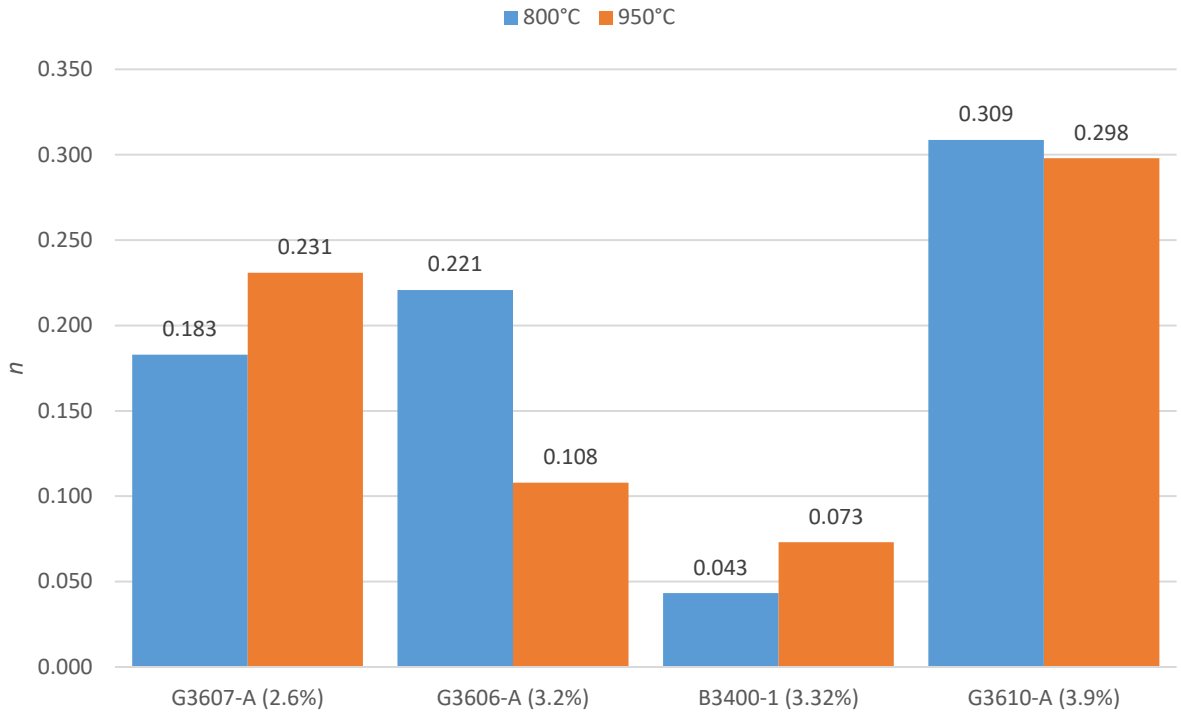

Figure 40: Histogram of n values as a function of wt% Al

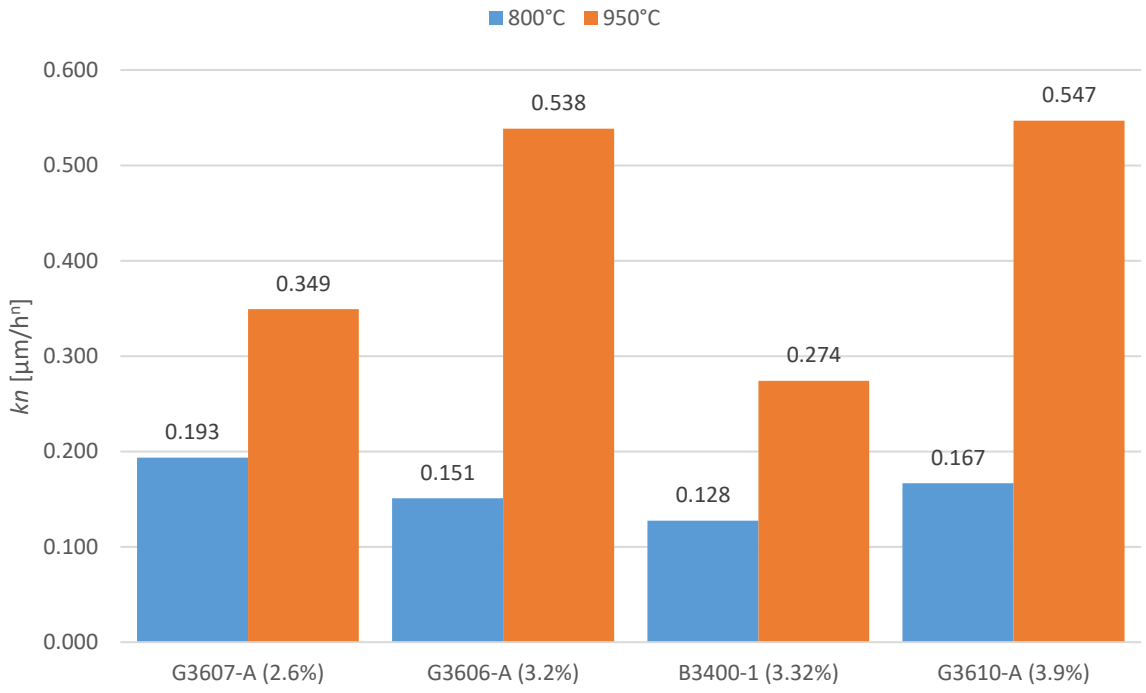

Figure 41: Histogram of kn values as a function of wt% Al

4.3 Prediction of oxide layer thickness

In order to use the results from the calculation of *kp* values, the experimental thickness equation was plotted. This produced Figure 42 which is capable of predicting the average thickness that would develop for a given alloy, time and temperature based on the assumed value of *n* at ½ in accordance with Wagner's model.

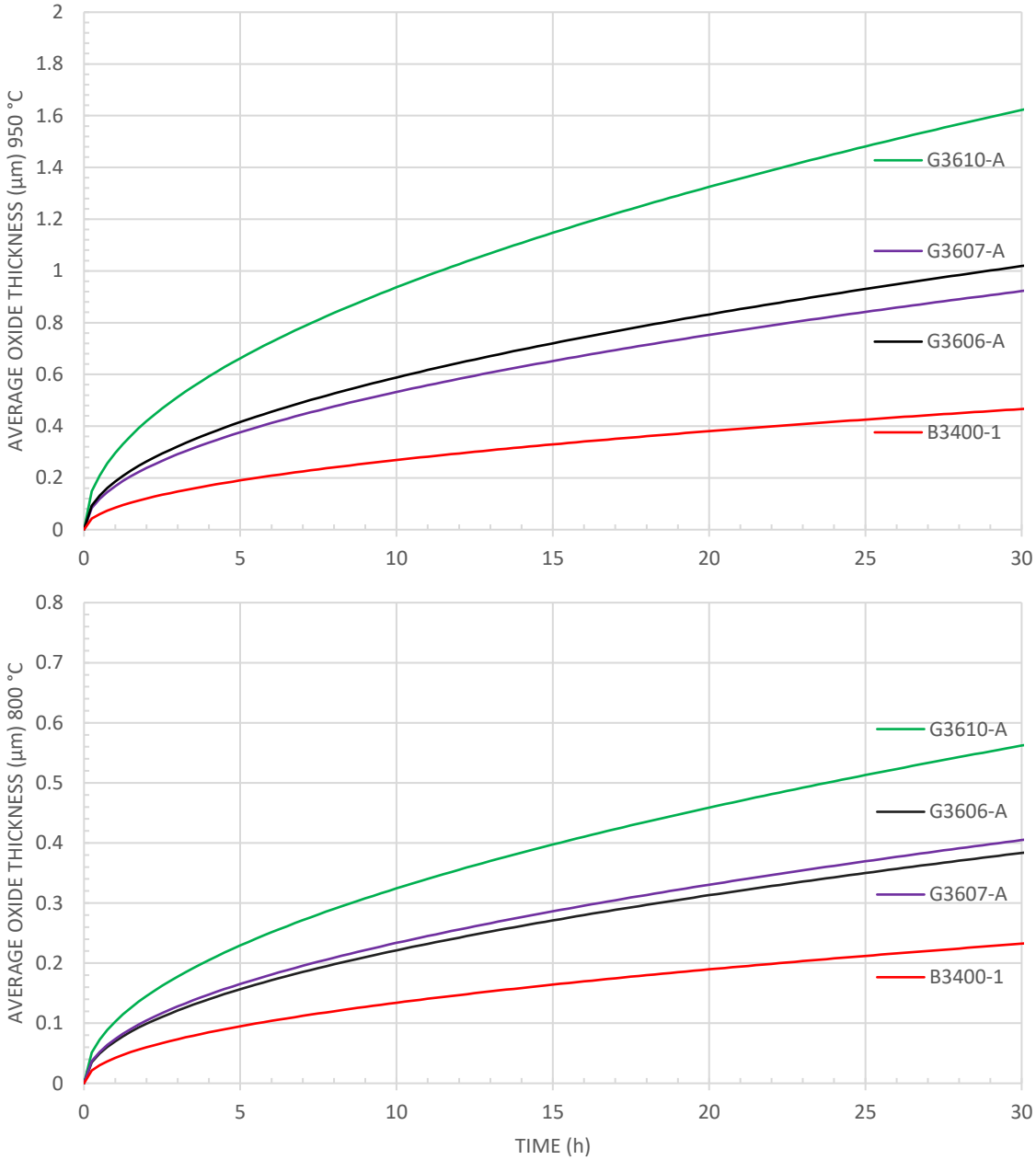

Figure 42: Prediction chart of average thickness of alumina using Wagner model

Additionally, each value of the *kn* was used to calculate a theoretical value for the average thickness developed on each alloy after a given time in a specified temperature based on modifications to the Wagner model. The chart shown in Figure 43 allows for such predictions out to thirty hours.

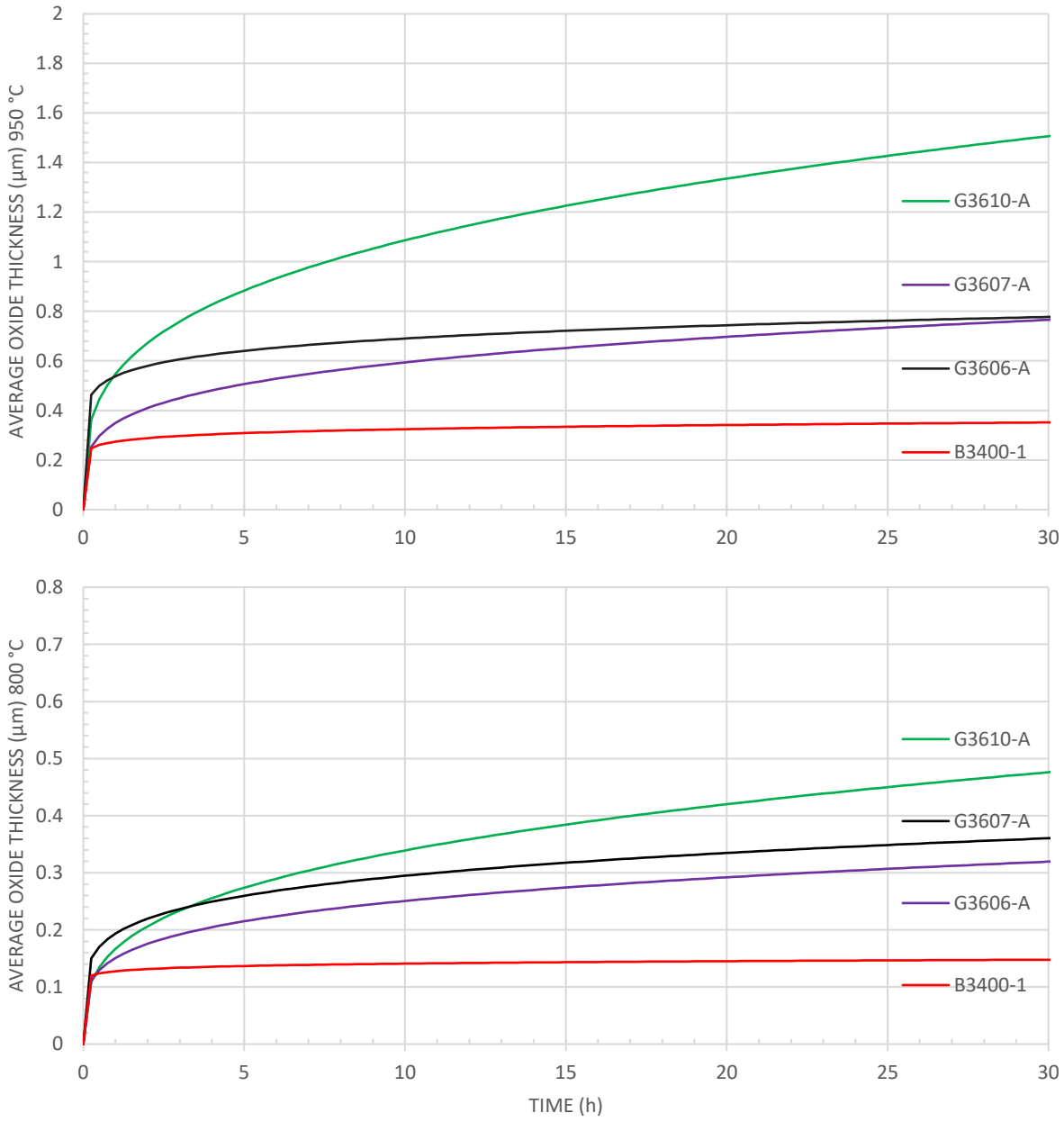

Figure 43: Prediction chart of average thickness of alumina using kn values

An example of the difference in predicted average oxide layer resulting from the Wagner model *kp*, and the experimentally determined *kn* rate equations can be seen in Figure 44. If each alloy were to follow the *kn* rate equation it would be beneficial, as oxide layer develops at a much greater rate, allowing for less required oxidation time to achieve a constant thickness.

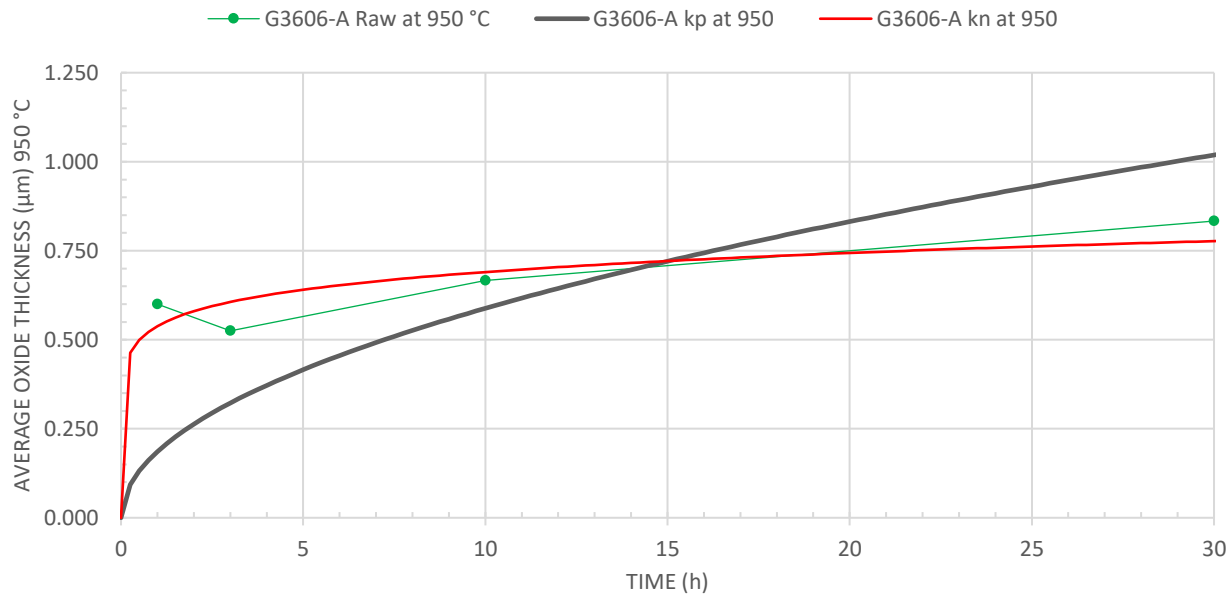

Figure 44: Comparison of kp to kn thickness predictions for G3606-A (3.2%) at 950 °C

CHAPTER 5 – CONCLUSIONS

New alloys of alumina forming austenitic stainless steel have recently been investigated as replacements for chromia forming alloys currently used in the petrochemical industry. These alloys contain between 2.6 and 3.9 wt% aluminum with large quantities of nickel to counteract the ferritic promoting properties of aluminum. Alumina forming alloys are a desirable alloy for investigation due to their more chemically and thermodynamically stable oxide layer in the presence of aggressive species formed in petrochemical steam cracking plants. Therefore, experiments were performed to investigate the oxidation kinetics of these alloys in the presence of pure steam.

Samples were oxidized using a tube furnace and steam generator system, which allowed for the production of a pure steam environment. These samples were then subjected to various temperatures and oxidation times in an effort to develop oxidation kinetic oxidation models.

Oxidation kinetics were tracked with mass changes and measurement of oxide layer thickness. Samples were examined using various characterization techniques including Raman, SEM, EDS and optical spectrometry for effects of the oxidation process. Examination focused on the effects of steam on the inner-diameter of the samples, and the overall thickness of oxide developed during oxidation.

Based on results from Raman spectroscopy and SEM it was determined that samples developed a continuous layer of aluminum oxide on their surfaces. The oxide layer was seen to be free of cracks and defects from SEM imaging, however it was seen that at temperatures of 950 °C the outer-diameter of samples showed the presence of internal oxidation. No internal oxidation was observed on any samples processed at 800 °C, nor on the ID of any of the samples regardless of processing temperature. Therefore, it can be concluded that the presence of pure

steam did not negatively affect the oxide layer or base metal of which was seen in other research endeavors.

From the measured alumina thicknesses, calculated parabolic and modified oxidation rates, and developed prediction charts it can be concluded that the oxidation of alumina does not closely follow Wagner's parabolic model. Comparison of the rate constants between Wagner's model and experimental findings show a dramatic increase in the predicted oxide layer thickness. This is believed to be a result of interactions of the oxide layer with the concentrated steam environment and exclusion of microstructural effects from the Wagner model.

Developed oxidation curves for these selected alloys will be of benefit in future research as they will allow for the general idea of how long an oxidation process will require to develop a continuous oxide layer of substantial thickness. The benefit of these charts could be the ability to more accurately define procedures for cleaning processes and pre-oxidation processes in petrochemical cracking plants due to knowledge of time requirements for alumina development. This would result in less downtime and increases in production efficiency.

CHAPTER 6 – FUTURE WORK

Because of the limitations of the setup developed for these experiments, the precise content of steam could not be measured. Instead it was relied upon the knowledge that the system was flooded with steam, and no other environment could exist. However, modifications to this setup including a controlled steam generation system would improve the accuracy of steam generation.

In addition to improving the oxidation setup, future investigation of alternate environments would be of great use. For example, if the environment could be controlled accurately enough to regulate steam generation to between 0 and 100 % steam, it would allow for further research as to how the steam directly effects the formation of alumina. Currently, these alloys have only been studied under environments of dry air, 3%, and 10% steam. Therefore, there exists a need for further studies into the range of 10% to 100% steam.

Additional testing of samples between 800 to 950°C would allow for the calculation of alumina activation energies. These values would be of benefit for analyzing the true makeup of the oxide layer where a more advance analysis technique would allow for the identification of amalgams and more exotic compounds. These compounds could exist as ternary aluminum-iron-nickel systems of which Raman or XRD would struggle in identifying.

In further replicating conditions found in the petrochemical industry, testing is needed to determine the fatigue resistance of the developed alumina layer depending on thermal and chemical cyclic processing. Additionally, analysis of the effects that alumina layer thickness play in preventing the effects of coking are needed.

REFERENCES

1. *Coke Formation Reduction in the Steam Cracking of Naphtha on Industrial Alloy Steels Using Sulfur-Based Inhibitors.* Darioush Salari, Aligholi Niaei, Mohammad Reza Shoja, Reza Nabavi. A130, January 2010, INTERNATIONAL JOURNAL OF CHEMICAL REACTOR ENGINEERING, Vol. 8.

2. *Investigation of Coke Formation in Steam Cracking of Atmospheric Gasoil.* Abghari, Sorood Zahedi. 2, 2013, Journal of Petroleum Science Reaserch (JPSR), Vol. 2.

3. *Deployment of Alumina Forming Austenitic (AFA) Stainless Steel.* Michael P. Brady, Yukinori Yamamoto, Govindarajan Muralidharan, Hiram Rogers and Bruce A. Pint. Oak Ridge, TN : Oak Ridge National Laboratory, September 30, 2013.

4. Schoeller, Harry E. *Thermodynamics and Kinetics of Oxidation and Temperature Dependent Mechanical Characterization of Pure Indium Solder.* Binghamton : State University of New York, 2007. pp. 24-38. 0549335757.

5. Mott, N. Cabrera & N.F. *THEORY OF THE OXIDATION OF METALS.* s.l. : H. H. Wills Physical Laboratory, University of Bristol. pp. 163-181.

6. *High-temperature Oxidation-resistant Coatings: Coatings for Protection from Oxidation of Superalloys, Refractory Metals, and Graphite.* Coatings, National Research Council (U.S.). Committee on. s.l. : National Academies, 1970, p. 223.

7. Khanna, A. S. *Introduction to High Temperature Oxidation and Corrosion.* s.l. : ASM International , 2002. 0871707624.

8. Samal, Sneha. High-Temperature Oxidation of Metals. [book auth.] Zaki Ahmad. *High Temperature Corrosion.*

9. *Modeling of $\theta \rightarrow \alpha$ alumina lateral phase transformation with applications to oxidation kinetics of NiAl-based alloys.* Xin Liang, Xinwei Wang. s.l. : Journal of Materials and Design, 2016, Vol. 112.

10. *Development of Cast Alumina-Forming Austenitic Stainless Steels.* G. MURALIDHARAN, Y. YAMAMOTO, M.P. BRADY, L.R. WALKER. s.l. : JOM, 2016, Vol. 68.

11. BRUCKNER, JÜRGEN. Considering thermal processes for dissimilar metals. *TheFabricator.com.* [Online] 2003. [Cited: 11 21, 2016.] http://www.thefabricator.com/article/metalsmaterials/considering-thermal-processes-for-dissimilar-metals.

12. Iron-Nickel (Fe-Ni) Phase Diagram. *Computational Thermodynamics.* [Online] 2008. [Cited: 11 21, 2016.] http://www.calphad.com/iron-nickel.html.

13. Valérie Mousseaux, Paris, Francois Ropital, Malmaison and André Sugier, LeCros de Cagnes, all of France. *PROCESS FOR USING ANTI-COKING STEELS FOR DIMINISHING COKING IN A PETROCHEMICAL PROCESS. 5,693,155* USA, dec. 2, 1997.

14. *Composition, Microstructure, and Water Vapor Effects on Internal/External Oxidation of Alumina-Forming Austenitic Stainless Steels.* M.P. Brady, Y. Yamamoto, M.L. Santella, L.R. Walker. s.l. : Oxidation of Metals, 2009, Vol. 72.

15. *Water-Vapor-Effect on the Oxidation of Fe--21.5 wt.%Cr-5.6 wt.%A1 at 1000°C.* H. Buscail, S. Heinze, Ph. Dufour, and J. P. Larpin. s.l. : Oxidation of Metals , 1997, Vol. 47.

16. *Development of Alumina-Forming Austenitic Stainless Steels* . Yamamoto, Brady, Santella, Bei, Maziasz, Pint. Clearwater, Fl : 33rd International Technical Conference on Coal Utilization & Fuel Systems, 2008.

17. Raman Explained. *Renishaw apply inovation.* [Online] Renishaw. [Cited: 11 20, 2016.] http://www.renishaw.com/en/raman-spectroscopy-in-more-detail--25806.

18. *Oxidation of alloys containing aluminum and diffusion in Al 2 O 3.* Doremus, Robert H. s.l. : Journal of Applied Physics, 2004, Vol. 92.

19. Larsen, Kathy Riggs. Alumina-Forming Austenitic Alloys Resist High-Temperature Corrosion. *Materials Performance.* [Online] 10 7, 2016. [Cited: 11 21, 2016.] http://www.materialsperformance.com/articles/material-selection-design/2015/12/alumina-forming-austenitic-alloys-resist-high-temperature-corrosion.

APPENDIX A: Full Composition of Alumina Alloys

Determined prior to receipt from MetalTek via optical emission spectrometer

	Alloy			
Element	G3607-A	G3606-A	B3400-1	G3610-A
Al	2.62	3.2	3.23	3.9
B	0.001	0.001	0.017	0.002
C	0.425	0.43	0.428	0.436
Co	0.0417	0.0525	0.2571	0.0431
Cr	27.9996	27.5958	31.0537	27.396
Cu	0.0329	0.032	0.0426	0.0353
Fe	26.8481	27.0002	17.2265	24.9261
Mn	0.783	0.795	0.141	0.795
Mo	0.171	0.179	0.212	0.188
N	0.0403	0.0374	0.0623	0.0305
Nb	0.7398	0.7298	0.5346	0.747
Ni	38.2575	37.9573	45.5928	38.0119
O	0.0006	0.0003	0.0018	0.0005
P	0.014	0.014	0.01	0.015
S	0	0.003	0	0
Si	1.3012	1.3204	0.3506	1.4143
Sn	0	0.001	0	0.001
Ti	0.108	0.115	0.095	0.118
V	0.042	0.04	0.042	0.041
W	0.409	0.317	0.557	1.669
Zr	0.115	0.13	0.107	0.13

APPENDIX B: Sample EDS Output Report

Application Note
Company / Department

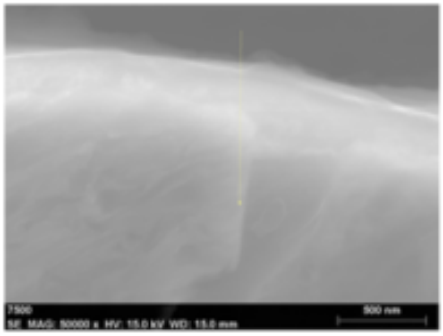

7500_SEDate:10/20/2016 12:23:09 PMImage size:1500 x 1125Mag:50000xHV:15.0kV

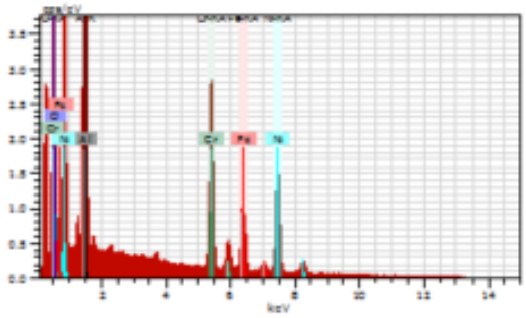

Scan Date:10/20/2016 12:23:42 PM HV:15.0kV
Puls th.:6.20kcps

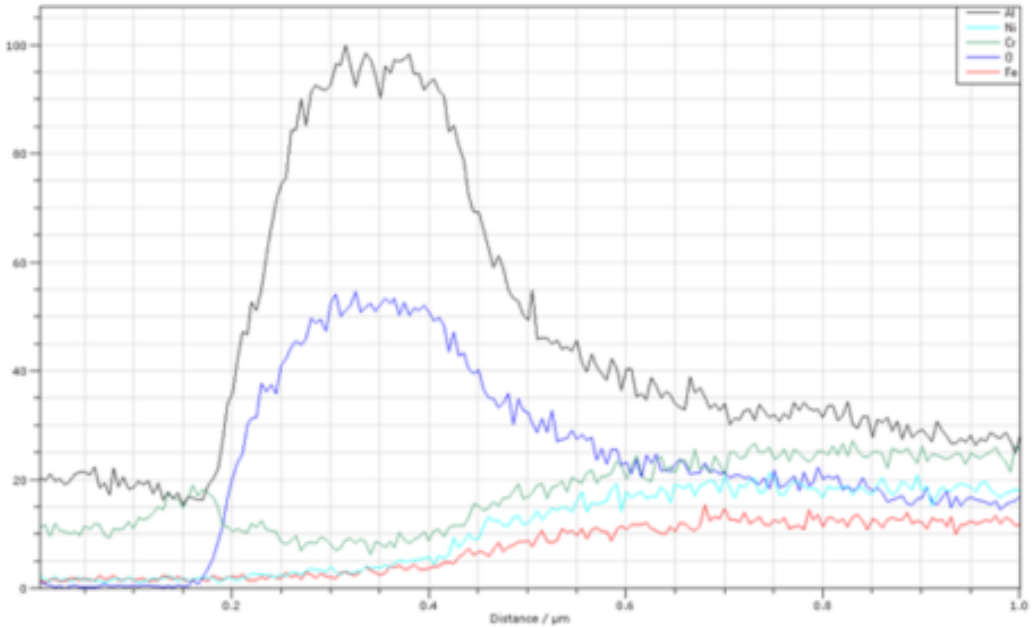

Line scan 1Date:10/20/2016 12:26:31 PMMeasure time:2:30 minStart:(816,88) End:(811,694)Length:1 µm

APPENDIX C: Tabulated alumina thickness measurements

#.1 = where oxide layer was deemed to start

#.2 = where oxide layer was deemed to end

= difference between #.1 & #.2

*some samples were only measured in 2 locations

G3607-A 800 °C										
	Thickness (μm)									
Time (h)	1.1	1.2	1	2.1	2.2	2	3.1	3.2	3	AVG.
1	0.250	0.400	0.150	0.300	0.525	0.225	-	-	-	0.188
3	0.200	0.300	0.100	0.075	0.200	0.125	0.150	0.250	0.100	0.108
10	0.150	0.400	0.250	0.150	0.475	0.325	0.350	0.750	0.400	0.325
30	0.175	0.575	0.400	0.275	0.550	0.275	-	-	-	0.338
G3607-A 950 °C										
	Thickness (μm)									
Time (h)	1.1	1.2	1	2.1	2.2	2	3.1	3.2	3	AVG.
1	0.150	0.625	0.475	0.100	0.400	0.300	-	-	-	0.388
3	0.250	0.700	0.450	0.275	0.725	0.450	0.225	0.525	0.300	0.400
10	0.200	0.725	0.525	0.200	0.750	0.550	0.100	0.675	0.575	0.550
30	0.250	1.150	0.900	0.300	1.075	0.775	-	-	-	0.838

G3606-A 800 °C										
	Thickness (μm)									
Time (h)	1.1	1.2	1	2.1	2.2	2	3.1	3.2	3	AVG.
1	0.250	0.425	0.175	0.200	0.350	0.150	-	-	-	0.163
3	0.150	0.300	0.150	0.225	0.425	0.200	-	-	-	0.175
10	0.100	0.350	0.250	0.100	0.475	0.375	0.200	0.300	0.100	0.242
30	0.175	0.475	0.300	0.125	0.500	0.375	-	-	-	0.338
G3606-A 950 °C										
	Thickness (μm)									
Time (h)	1.1	1.2	1	2.1	2.2	2	3.1	3.2	3	AVG.
1	0.150	0.800	0.650	0.150	0.700	0.550	-	-	-	0.600
3	0.125	0.550	0.425	0.125	0.750	0.625	0.200	0.725	0.525	0.525
10	0.100	0.800	0.700	0.100	0.775	0.675	0.150	0.775	0.625	0.667
30	0.250	0.900	0.650	0.250	1.100	0.850	0.200	1.200	1.000	0.833

B3400-1 800 °C										
	Thickness (μm)									
Time (h)	1.1	1.2	1	2.1	2.2	2	3.1	3.2	3	AVG.
1	0.225	0.375	0.150	0.275	0.375	0.100	-	-	-	0.125
3	0.250	0.575	0.325	0.275	0.500	0.225	0.175	0.475	0.300	0.283
10	0.375	0.475	0.100	0.275	0.475	0.200	-	-	-	0.150
30	0.050	0.200	0.150	0.150	0.300	0.150	0.050	0.175	0.125	0.142
B3400-1 950 °C										
	Thickness (μm)									
Time (h)	1.1	1.2	1	2.1	2.2	2	3.1	3.2	3	AVG.
1	0.175	0.450	0.275	0.175	0.475	0.300	-	-	-	0.288
3	0.075	0.325	0.250	0.075	0.350	0.275	0.175	0.425	0.250	0.258
10	0.150	0.525	0.375	0.150	0.525	0.375	-	-	-	0.375
30	0.275	0.600	0.325	0.250	0.600	0.350	0.175	0.500	0.325	0.333

G3610-A 800 °C										
	Thickness (μm)									
Time (h)	1.1	1.2	1	2.1	2.2	2	3.1	3.2	3	AVG.
1	0.100	0.275	0.175	0.100	0.250	0.150	-	-	-	0.163
3	0.150	0.425	0.275	0.125	0.425	0.300	-	-	-	0.288
10	0.200	0.450	0.250	0.175	0.400	0.225	-	-	-	0.238
30	0.175	0.800	0.625	0.100	0.575	0.475	0.150	0.750	0.600	0.567
G3610-A 950 °C										
	Thickness (μm)									
Time (h)	1.1	1.2	1	2.1	2.2	2	3.1	3.2	3	AVG.
1	0.075	0.500	0.425	0.100	0.550	0.450	-	-	-	0.438
3	0.600	1.600	1.000	0.500	1.600	1.100	0.500	1.450	0.950	1.017
10	0.200	1.400	1.200	0.300	1.450	1.150	-	-	-	1.175
30	0.300	1.600	1.300	0.200	1.500	1.300	-	-	-	1.300